SYNTHESIS AND CHARACTERIZATION OF COBALT-BASED MAGNETIC NANOSTRUCTURES

by

JACOB ELKINS

Presented to the Faculty of the Graduate School of

the University of Texas at Arlington in Partial Fulfillment

of the Requirements

for the Degree of

MASTER OF SCIENCE IN MATERIALS SCIENCE AND ENGINEERING

THE UNIVERSITY OF TEXAS AT ARLINGTON

August 2020

ABSTRACT

SYNTHESIS AND CHARACTERIZATION OF COBALT-BASED MAGNETIC NANOSTRUCTURES

Jacob Elkins, M.S.

The University of Texas at Arlington

Supervising Professor: J. Ping Liu

Co is an attractive element in the development of nanostructured magnetic materials due to its relatively high moment (1.72-1.75 μ_B) and strong exchange and spin-orbit interactions, and many of these materials have potential in applications such as data recording media, hyperthermia treatments, and nanostructured permanent magnets. In this thesis, magnetic nanostructures of $CoFe_2O_4$, Co, and CoNi with controlled size, shape, composition, and crystal structure are synthesized via bottom-up wet chemical methods and their magnetic properties are systematically characterized. Additionally, nanocomposites of exchange-coupled FeCo/$CoFe_2O_4$ and Co/FeCo core-shell nanostructures with enhanced magnetizations are prepared and investigated. In order to understand the prominent surface effects, $CoFe_2O_4$ nanoparticles are investigated by comparing nanoparticles of sizes 3.5 nm and 16 nm. It is found that the 3.5 nm nanoparticles in an assembly have a coercivity of 23 kOe at 5 K, which is attributed to the exchange coupling of the core spins to the surface disordered spins. The magnetization value is enhanced to 108 emu/g by synthesizing FeCo/$CoFe_2O_4$ core-shell nanocomposites of size 10.5 nm, and compared to pure $CoFe_2O_4$ nanoparticles, these core-shell nanoparticles are shown to have enhanced dipolar and exchange interactions. More importantly, the alignment of these nanoparticles in an assembly is shown to have a significant effect on the coercivity, reaching as high 22.4 kOe at 10 K for an assembly

aligned under an external field. Co nanowires were synthesized using a thermal decomposition method, and their diameters were controlled by varying the concentration of surfactant. A diameter as low as 10 nm was achieved and the coercivity reached 10.4 kOe for an aligned assembly. The 10 nm nanowires were then coated with FeCo using an electroless plating method, which increased the magnetization saturation from 150 emu/g for the pure Co to a max of 182 emu/g for the Co/FeCo nanocomposite. In addition to the Co nanowires, $Co_{1-x}Ni_x$ nanowires and nanoparticles were synthesized using a solvothermal approach. The Ni concentration was varied by controlling the Ni precursor concentration. The effects of the Ni concentration on the morphology, structure, and magnetic properties are investigated. Systematic investigation of the nanoparticles shows that the CoNi can retain nanowire morphology and hcp crystal structure up to a 30% Ni concentration, with further increase of Ni leading to the growth of polyhedral fcc nanoparticles. The magnetic performance of the CoNi nanoparticles with varying Ni concentration in assemblies is then investigated.

ACKNOWLEDGEMENTS

I would like to express my sincere gratitude to my advisor Dr. J. Ping Liu for providing guidance, knowledge, and resources throughout my research and studies. His supervision has helped me develop the necessary skills to design and manage research projects and coordinate with other members of the team. I would like to thank Dr. Jeotikanta Mohapatra, who has not only taught me invaluable knowledge and skills in the lab but has also provided support as a friend. I would also like to thank my colleagues Meiying Xing and Julian Beatty for their contributions, ideas, and cooperation in my lab activities.

I am thankful to Dr. Yaowu Hao for teaching me about magnetic materials, which has helped me in my research. I would also like to thank him for serving on my thesis supervising committee and providing suggestions to improve my thesis.

I would like to give special thanks to all of my friends and family, who have provided unwavering love and support throughout all of my endeavors.

Finally, I would like to give thanks to my father, Dr. Kevin Elkins who was the first to inspire me to study in the field of nanotechnology.

TABLE OF CONTENTS

LIST OF FIGURES

CHAPTER 1 Fundamentals of Magnetism and Magnetic Materials

1.1 Basic Principles

Magnetism was first discovered in early civilization when people found that lodestone, a natural mineral composed of magnetite, was attracted to iron through an unseen force that later became known as magnetism. As the lodestone was explored, it was found that the Earth itself had a magnetic field and the lodestone was consequently used to make early magnetic compasses by China in the 12th Century. [1] Several years later after the introduction of electricity, it was found that an electric current also produces magnetic fields, which sparked the research that led to many electrostatic and magnetostatic relations that were unified into the Maxwell relations. While these relations were derived from an electrostatic point of view, there are many parallels that can be drawn between magnetism from an electric current to the magnetism of a material and thus are useful in providing an understanding of how magnetism originates in a magnetic material.

1.1.1 Quantities and Units

The atom can be envisioned, in a very simplified model, as an electron orbiting the nucleus. The magnetic properties arise primarily from two components of the electron: the orbital motion and the spin. The nucleus will also have a small contribution, but the magnitude of its magnetic properties is very small compared to the electron contribution and it is usually ignored. To relate the atom to an electrostatic description, the orbital motion can be described as a circular loop of wire carrying a current, as seen in Figure 1.1. From here it is possible to derive the magnetic properties of a material using the electrostatic relations.

Figure 1.1 (a) The moment of a loop of wire carrying a current and (b) the moment of an electron in a hydrogen atom.

Starting with a simple case, the magnetic field flux density (*B*) generated by the motion of the electrons along a wire can be described by the Biot-Savart Law

$$B(r) = \frac{\mu_0}{4\pi}\int \frac{IdL \times r}{|r^3|} \quad \text{(T)} \tag{1.1}$$

where μ_0 is the permeability of free space, *dL* is a segment of the wire, *r* is the displacement vector, and *I* is the current.[2] Often when discussing magnetism, the magnetic flux is expressed in terms of the magnetic field *H*, and in SI units the magnetic flux density in air is related to the magnetic field (*H*) by[3]

$$B = \mu_0 \mathrm{H} \tag{1.2}$$

If a length of wire is fashioned into a circular loop like in Figure 1.1, the magnetic field in the center of the loop along the radial axis can be derived from eq 1.1 and 1.2 so that

$$H(r) = \frac{I}{2R} \tag{1.3}$$

where *R* is the radius of the loop. A current carrying loop also has another easily described quantity known as the magnetic moment, which is expressed as

$$m = IA \tag{1.4}$$

where *A* is the area of the loop.[2] When discussing magnetic materials, this value is usually expressed in units of the Bohr Magneton μ_B = 9.27 x 10^{-24} Am^2, which is derived from the Bohr

atomic model of an atom with a single electron. Since this model assumes that the electron orbits the atom, the atomic magnetic moment can be expressed in terms of the total momentum of the electron. In fact, the moment of an atom is more accurately determined from the quantum mechanical description of the angular momentum of the orbit and spin momentum. The total magnetic moment from the electron orbit and spin in terms of quantum mechanical momentum can be derived to give

$$m = \frac{eh}{4\pi m_e} g_L \sqrt{J(J+1)} \tag{1.5}$$

where e is the electric charge of an electron, m_e is the mass of an electron, h is Planck's constant, g_L is the Landé factor, and J is the total angular momentum quantum number (the sum of the total spin momentum S and total orbital momentum L quantum numbers).[4]

Another important case worth investigation is the solenoid, in which a wire is tightly coiled in a helical fashion. It is often approximated as a series of stacked loops with a uniform number of loops (N) per unit length (l), with $n = N/l$. Here it is more beneficial to use Ampere's Law which states that the line integral of the magnetic flux density around a closed loop is proportional to the enclosed current[2]

$$\oint B * d\mathbf{s} = \mu_0 I \tag{1.6}$$

Using this relation and a selected closed loop, the magnetic field inside an infinite solenoid is described by

$$B = \mu_0 nI = \mu_0 K \tag{1.7}$$

where K is the surface current, or current per unit length.

Since the atom can be considered as a current carrying loop, and any material is built out of many atoms, the magnetic material can be considered as a collection of N loops. Each of these loops will act as a magnetic dipole and have a magnetic moment, and assuming that all of the

moments are aligned in one direction, the number of magnetic moments per unit volume of the material can be defined as the Magnetization *M*, so that

$$M = \frac{Nm}{V} \qquad 1.8$$

where *V* is the volume of the material.[3] For simplicity, the material is assumed to be in the shape of a cylinder, so that the loops will always have an adjacent loop that will cancel their current contribution, with the exception of the outermost loops. This can be approximated to a net current on the surface and the magnetic material resembles a solenoid with area *A*, which is illustrated in Figure 1.2.[5]

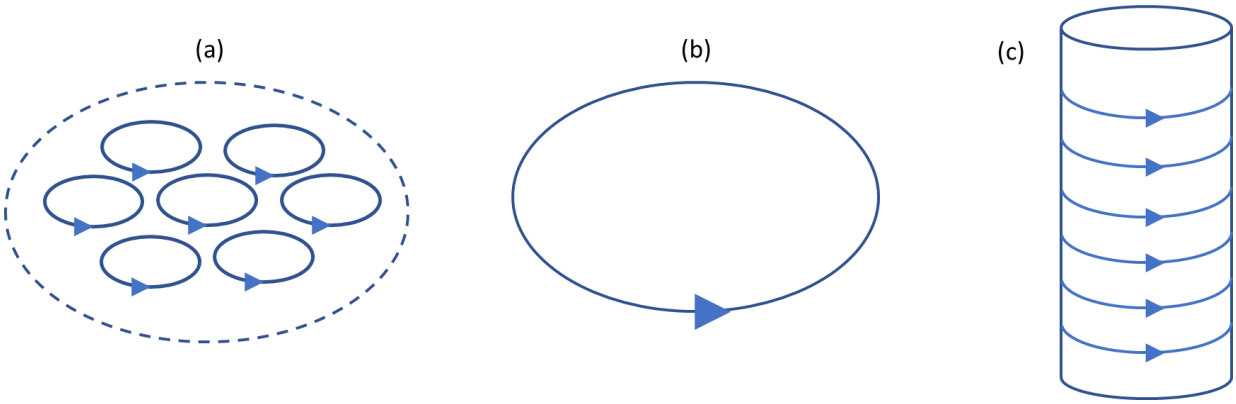

Figure 1.2(a) Shows how the atoms in a cylindrical magnetic material can be treated as a collection of loops which will have the same net moment as (b) a single large loop. The material can then be treated as a solenoid similar to (c).

The magnetic field can then be found similar to the way it was found for the solenoid, however, the moment produced by the net current I_N can be equated to the net moment of the collection of loops

$$I_N A = Nm \qquad 1.9$$

so that

$$I_N = \frac{Nm}{A} \tag{1.10}$$

and the equation for the magnetic flux density becomes

$$B = \mu_0 K = \mu_0 \frac{I_N}{L} = \mu_0 \frac{Nm}{AL} = \mu_0 M \tag{1.11}$$

When measuring the magnetic properties of materials, the magnetic flux density has an additional component, due to the external field used in the measurement, so that it is expressed as a sum

$$B = \mu_0 (H_a + M) \tag{1.12}$$

where H_a is the applied field.[3]

Another useful quantity is the magnetic susceptibility χ, which is the relationship of the magnetization to the magnetic field

$$\chi = \frac{\boldsymbol{M}}{\boldsymbol{H}} \quad \text{(volume)} \tag{1.13}$$

$$\chi_m = \frac{\boldsymbol{M}}{\rho \boldsymbol{H}} \quad (mass) \tag{1.14}$$

where ρ is the density of the material.[3]

Like many other units of measurement, there are multiple ways that these quantities can be expressed, and it would be useful to be aware of the other commonly used units. Typically, the two commonly used unit systems are the CGS and SI, which are summarized in Table 1.1.

Table 1.1 A summary of commonly used magnetic units and their conversion factors.

Quantity	SI	CGS	Conversion Factor	
Magnetic Flux Density (B)	Tesla (T)	Gauss (G)	10^{-4}	
Magnetic Field (H)	Ampere/meter (A/m)	Oersted (Oe)	$10^3/4\pi$	
Magnetization (M)	A/m	emu/cm^3	$10^3/4\pi$	
Magnetic Moment (m)	Am^2	emu	10^{-3}	
Susceptibility (χ)	Dimensionless	emu/Oe·cm^3	4π	
Energy Product $(BH)_{max}$	kKJ/m^3	GOe	$10^2/4\pi$	

1.1.2 Types of Magnetism

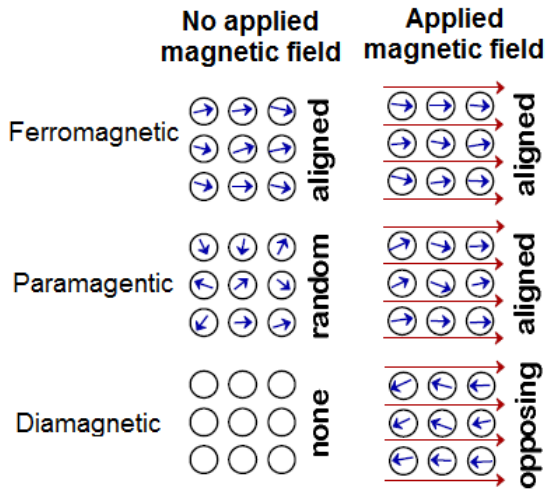

Figure 1.3 Demonstration of how the three main categories of magnetic materials respond to an external field. Ferromagnetic materials are initially aligned, and the alignment is slightly improved with an external field. Magnetic moments of a paramagnet are initially randomized, which can align in the same direction of an applied field. Diamagnetic materials have no initial moment but align antiparallel to an external field.[6]

All materials exhibit some form of magnetic behavior that originates from the spin and orbit of the electron. However, there are internal interactions that strongly affect the magnetic behavior and they can vary from one material to the next. While there are multiple types of magnetic behavior, most materials can be classified under the three main categories: diamagnetic, paramagnetic, and ferromagnetic. They are often easily identified by their susceptibility and magnetization, as well as the temperature dependence of some of their properties. The general interactions of these materials with and without an external field are summarized in Figure 1.3.

Diamagnetism is most common in materials with no net magnetic moment in absence of an external magnetic field. From a classical point of view, when the material is subjected to a

magnet field the electron orbit is affected so that the current of the orbital loop is reduced, and according to the Lenz Law, this causes the magnetic moments to align opposite of the applied field to compensate. Each atomic moment is assumed to be non-interacting, meaning each moment is independent and not influenced by other moments. This type of material is identified by having a susceptibility value that is negative, in fact, superconductors are considered perfect diamagnets with χ= -1. Additionally, there is no appreciable temperature dependence for the susceptibility. Most materials have some amount of diamagnetism due to having filled electron levels, however, it is often overpowered by more prominent magnetic behaviors such as paramagnetism or ferromagnetism.

In a **paramagnetic material**, each of the atoms contain a net magnetic moment of the same value due to unpaired valence electrons. With no external field, these moments are randomly oriented so that the moments are interatomically cancelled and the net moment of the material is zero. When a field is applied, some of the moments will align to the field direction to create a net moment. However, after removing the external field, the moments will randomize, and the net moment will return to zero. This is because thermal energy is often sufficient to overcome the energy required to move the moment out of alignment, causing the moments to randomize. Even with a strong external field, a paramagnetic material can only be partially aligned at room temperature. The mass susceptibility of a paramagnetic material was first shown by Pierre Curie to follow an inverse relationship with the temperature.[7] However, it was later shown that this relationship is a more specific case of the Curie-Weiss Law

$$\chi_m = \frac{C}{T-\theta} \qquad 1.15$$

where C is the Curie constant, T is the temperature in kelvins (K) and θ describes the amount of interaction. In a paramagnet, θ is either small or zero and can be positive or negative.[3]

In **ferromagnetic materials**, the magnetic moments of the atom are easily aligned in one direction and can be done with very low external fields. These materials can easily reach their maximum obtainable magnetization, or saturation magnetization, as long as the temperature is kept below its respective Curie temperature T_C. To understand why ferromagnets are easily magnetized, Weiss developed a concept that proposed in ferromagnetic materials there are strong exchange interactions amongst the atoms that lead to an internal molecular field that will help align the moments in a spontaneous fashion. This in turn led to the derivation of the Curie-Weiss law (eq. 1.15), where for ferromagnetic materials, $\theta = T_C$. When the temperature of a ferromagnetic material is increased above its T_C, it will behave as a paramagnet. To better understand the effect of temperature on the spontaneous magnetization of a ferromagnetic material, the Langevin function is used so that the relative magnetization can be expressed as

$$\frac{M}{M_0} = \coth(a) - \frac{1}{a}. \tag{1.16}$$

and if the material is not under an external field[3]

$$a = \frac{m\gamma M}{kT} \tag{1.17}$$

$$\frac{M}{M_0} = \frac{kTa}{m\gamma M_0}. \tag{1.18}$$

The equations are plotted in Figure 1.4, where it is seen that when the temperature is below the T_C the maximum possible magnetization occurs at the intersection of the Langevin function and the equation for relative magnetization. The magnetic moments will spontaneously align up to the point of intersection (P) for the given temperature. When the temperature is equal to the T_C, the

slope is equal to the Langevin function slope near the origin, which is approximately 1/3. At any temperature beyond the T_C the line does not intersect the Langevin function past the origin, so that there is no spontaneous magnetization.

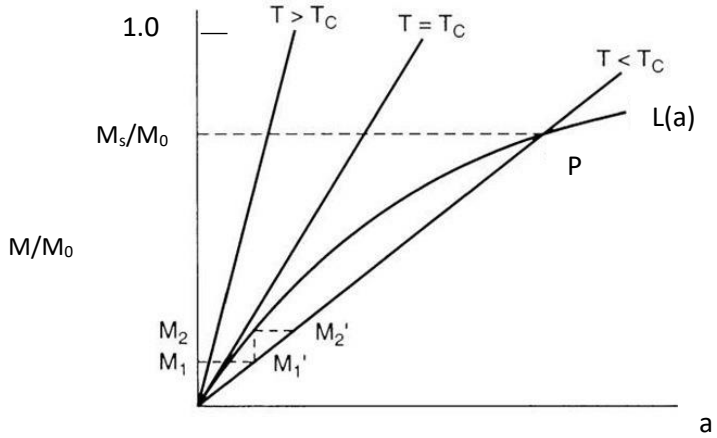

Figure 1.4 A plot of the Langevin Function *L(a)* and relative magnetization (eq. 1.18) as a function of *a*, at varying temperatures. Spontaneous magnetization occurs when there is an intersection between the Langevin function and eq. 1.18 (point P).[3]

Superparamagnetism is a subclass of paramagnetism that is worth discussing due to its important role in nanostructured magnetic materials. This behavior arises when the volume of single domain particles (which will be discussed in section 1.3.1) is reduced so that the thermal energy has a larger influence on the alignment of the magnetic moments. This essentially causes the particles to behave as a paramagnet, in absence of an external field. However, under an applied external field the particles will have a substantial magnetic moment compared to the moment of a paramagnet, hence the term superparamagnetic. Due to the large influence of thermal energy, the magnetic moments will tend to flip constantly for a given temperature. The average time it takes for the moment of the particle to flip is called the Neel relaxation time, and is given by

$$\tau = \tau_0 e^{KV/k_B T} \qquad 1.19$$

where K is the magnetic anisotropy constant, V is the particle volume, τ_0 is a constant typically equal to 10^{-9} sec, and k_B is the Boltzman constant.[3] The value of τ is often set to 100 sec (i.e. instrument measurement time) so that a temperature at which the magnetic moments of the particles remain stable can be defined, also known as the blocking temperature T_B. Using this value for τ and 10^{-9} sec for τ_0 the equation can be solved for the blocking temperature, so that[3]

$$T_B = \frac{KV}{25k}. \tag{1.20}$$

1.2 Properties of Ferromagnetism

Although there are multiple categories of magnetic materials, the vast majority of investigation and interest in magnetic materials is focused on ferromagnetic materials. Within the ferromagnetic category, there is a large degree of variation in the magnetic properties, thus necessitating more specific means of classifying a ferromagnetic material.

1.2.1 Magnetocrystalline Anisotropy

When dealing with ferromagnetic and nanostructured magnetic materials, it is often found that the direction at which the magnetic properties are measured has a considerable impact on their magnitude. This directional dependence on the magnetic properties is referred to as magnetic anisotropy and it is a very important concept in the design and manufacturing of commercial magnetic products. In crystalline magnetic materials, one of the largest contributing factors to the magnetic anisotropy is the crystal structure, thus the contribution to the magnetic anisotropy from the crystal structure is coined magnetocrystalline anisotropy. The magnetocrystalline anisotropy is primarily due to the interactions between the orbit and spin of the electrons, commonly referred to as spin-orbit coupling, and the magnetocrystalline energy is essentially the energy required to overcome the spin-orbit coupling. Additionally, the electron orbit is also strongly coupled to the

crystal lattice of the material, where the atomic arrangement influences the orientation of the orbit. Therefore, the crystal structure of magnetic materials will play an important role in creating preferred directions of magnetization.

Of the types of crystal structures, the cubic and hexagonal structures are the most common structures to consider. For the cubic system, the anisotropy energy is described using a series expansion so that

$$E_a = K_0 + K_1(\alpha_1^2\alpha_2^2 + \alpha_2^2\alpha_3^2 + \alpha_3^2\alpha_1^2) + K_2(\alpha_1^2\alpha_2^2\alpha_3^2) + \cdots \quad 1.21$$

where the K values are constants that are intrinsic properties of the material and α_1, α_2, α_3 are the directional cosines with respect to the crystal axes.[8] In a hexagonal close packed (hcp) crystal structure, the anisotropy energy is equal for all of the lateral planes (perpendicular to the c axis) so that the energy only depends on the angle with the c-axis, which can be expressed in terms of $sin\theta$ so that[8]

$$E_a = K_0 + K_1 sin^2\theta + K_2 sin^4\theta + \cdots \quad 1.22$$

The K_0, K_2, and higher order terms in the above equations (1.21 and 1.22) are often insignificant and typically ignored. The directions at which the energy is at a minimum will be the directions that can spontaneously magnetize to saturation. These directions are called the easy axes and the directions that require the most energy to magnetize are called the hard axes. Typically, magnetic materials with the cubic structure have multiple possible directions for the easy axis and tend to have less anisotropic magnetocrystalline behavior. For example, in bcc Fe the easy axis is along the <100> directions and the hard axis is in the <111> directions. In contrary, materials with the hcp crystal structure tend to only have one easy axis, referred to as uniaxial, and can have very anisotropic magnetic properties. For hcp Co, the easy axis lies along the <0001> directions and

the hard axis lies along the <1000> directions so that there is only one easy axis, making it one of the most anisotropic materials available. Although the magnetocrystalline anisotropy is strongly related to the crystal structure, magnetic anisotropy of alloys will have considerable dependence on the composition as well, and in some cases even change the easy axis directions without changing the crystal structure.[3,9]

1.2.2 Magnetic Domains

While ferromagnetic materials have preferred crystallographic directions in which they can spontaneously magnetize, in bulk ferromagnetic materials, such as iron, it is not uncommon to find little to no magnetic behavior in absence of an external field. It turns out that within bulk ferromagnetic materials, at a temperature below its T_C, there are localized regions of aligned magnetic moments known as magnetic domains, illustrated in Figure 1.5. As a whole, the net magnetic moment of the material is zero due to the cancellation of moments by the magnetic domains. The presence of magnetic domains in ferromagnetic materials is a result of competing energies that minimize the net magnetic energy, which can be expressed as a sum of four components

$$E_{tot} = E_a + E_{ex} + E_m + E_s \tag{1.23}$$

where E_a is the anisotropy energy, E_{ex} is the exchange energy, E_m is the magnetostatic energy, and E_s is the magnetoelastic energy.[10] The exchange energy comes from the exchange interactions of neighboring electron spins whose magnitude is related to the angle between two spins, preferring a parallel or antiparallel alignment. The magnetostatic energy describes the energy between a magnetic dipole and an external field, and the magnetoelastic energy is the energy involved in a

mechanically strained system. In many cases, the magnetoelastic energy is insignificant due to little or no strain in the magnetic material.

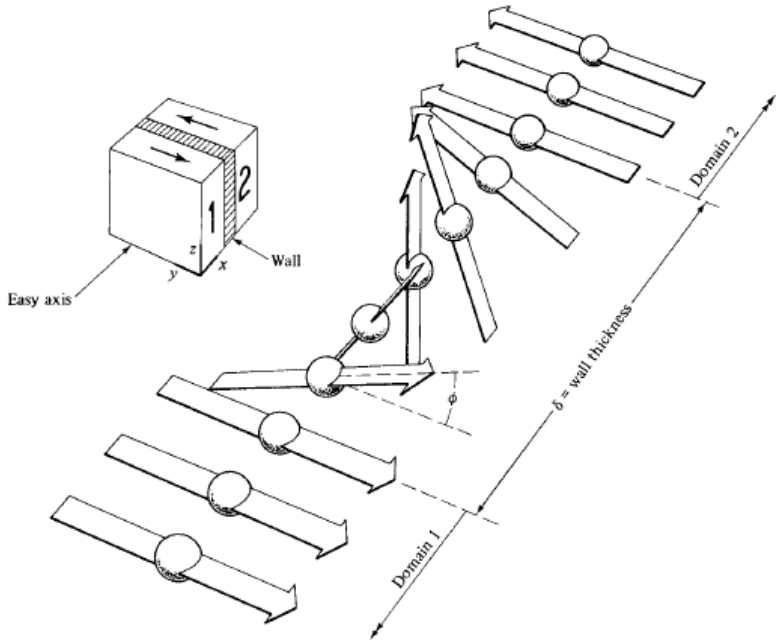

Figure 1.5 Two magnetic domains are separated by a transitional region where the magnetic moments gradually change their direction from one domain to the next. The transitional region that separates the domains is known as the domain wall. [3]

Adjacent magnetic domains are separated by a transitional region in which the magnetic moments gradually change direction, rather than abruptly switching at some interface, illustrated in Figure 1.5. This region is called the domain wall, and the thickness depends on the anisotropy energy and exchange energy of the material. The exchange energy is related to the angle between neighboring moments so that

$$E_{ex} = -2Acos(\frac{d\phi}{dx}) \qquad 1.24$$

where ϕ is the angle and A is an exchange constant.[3] The exchange energy attempts to keep the moments parallel, and to minimize the exchange energy, the moments change their directions in small increments. However, the anisotropy energy prefers that the moments remain in the easy directions and resists the changing directions of the moments as they move towards the hard axes. Therefore, the exchange energy will lead to wider domain walls while the anisotropy energy will work to shorten the walls. In most bulk ferromagnetic metals, the domain walls will be only a few hundred atoms thick.

1.2.3 Hysteresis Loops

While the domain walls in a ferromagnetic material can prevent magnetization of the moments to one direction, it can be overcome by the application of an external field. The external field will induce domain wall motion so that the magnetization increases along the direction of the applied field, reducing the size and number of domains not aligned to the field. The reorientation of the magnetization is not reversible in ferromagnetic materials upon removal of the external field and requires an applied field to return it to a demagnetized state, after being magnetized. When the response of the magnetization to the applied field is plotted, the additional field required to revert the magnetization will lead to a loop known as a hysteresis loop, similar to those in Figure 1.6. The hysteresis loop provides a lot of information about a magnetic material and it is often used to define three important magnetic properties: magnetization saturation (M_S), remanence magnetization (M_R), and coercivity (H_C). The M_S of a material is the maximum possible magnetization for a material, i.e. the point on a hysteresis loop where the value of M no longer increases with increasing applied field. The M_R is the magnetization that remains after the applied field is removed (when $H_a = 0$), and the H_C is the value of H_a that demagnetizes the material so

that M = 0. Considering only magnetocrystalline anisotropy, the H_C of a crystalline magnetic material can be calculated from[3]

$$H_C = \frac{2K_1}{M_S} \tag{1.25}$$

It should be noted that it is not necessary to consider K_0 since it remains constant, and K_2 is often negligible.

In addition to finding important magnetic quantities, the hysteresis loops are also used to further classify ferromagnetic materials into two sub-classes: soft magnets and hard magnets. Soft magnets are often accompanied by loops with a low area, as seen in Figure 1.6, and their direction of magnetization is easily changed. On the contrary, hard magnets have a much larger loop area and can be much more difficult to change the direction of magnetization once magnetized. Hard magnetic materials are a necessary component in permanent magnets, and their effectiveness is often characterized by a quantity known as the energy product, or $(BH)_{max}$, which is expressed as

$$(BH)_{max} = 1/V \int |B \cdot H| dr \tag{1.26}$$

The $(BH)_{max}$ is dependent on both the M_R and H_C, however, it cannot exceed $\mu_o M_R^2/4$ which would be an ideal rectangular hysteresis loop.[11] The $(BH)_{max}$ is typically determined from a B-H hysteresis plot and corresponds to the largest possible rectangular area under the curve, as shown in Figure 1.6c.

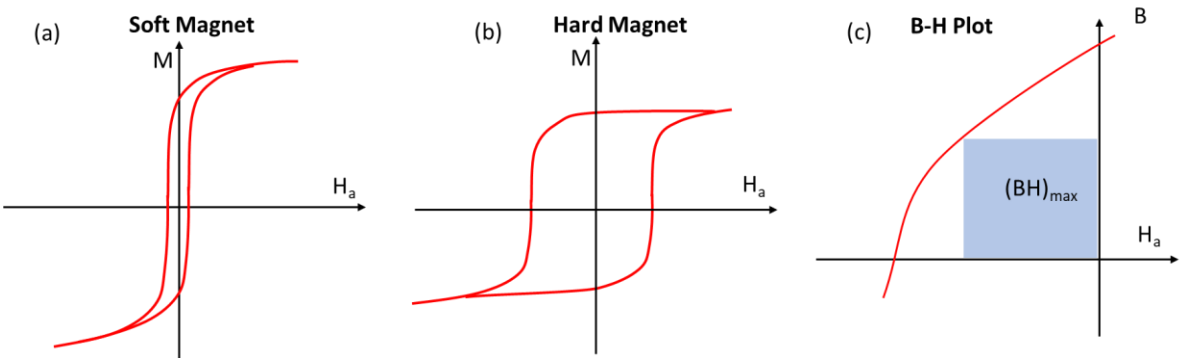

Figure 1.6 Example hysteresis loops for (a) soft and (b) hard magnetic materials. (c) Example B-H plot in the second quadrant and the region of the maximum energy product $(BH)_{max}$.

1.3 Nanostructured Magnetic Materials

While nanotechnology and the use of nanostructured materials is a relatively new and rapidly developing field, magnetic nanomaterials have been found to exist in nature and have played important roles for many organisms for hundreds of years. One of the most interesting examples is the presence of magnetite nanocrystals in magnetoreceptors of trout, which is believed to play a role in the long range migratory navigation using the Earth's magnetic field.[12] However, it wasn't until the 20th century, when nanoscience was being advocated by Richard Feynman in talks such as "There's Plenty of Room at the Bottom," that a broad investigation of nanotechnology started to take hold. Since then, many tools have been developed to allow images of materials down to the atomic scale that has vastly aided the development of nanomaterials. It has been found that in the nano-regime, many features such as size and shape become profoundly important to the properties of the material, and nanostructured materials have established a broad range of applications throughout emerging technologies. In particular, nanostructured magnetic materials have been demonstrated to have potential in high-density data storage, cancer therapies, and

nanostructured permanent magnets. Thus, there has been considerable interest in the development of nanostructured magnetic materials.

1.3.1 Size Effects

In bulk materials, the magnetic properties are largely defined by the composition, crystal structure, magnetic anisotropy, and defects. As the size of the material is decreased to the nano-regime, differences in size can have much more pronounced effects on the magnetic properties of ferromagnetic materials. Due to how much of an effect the size can have on the magnetic properties of a material, it is often the first parameter considered in the design of nanostructured magnets. Starting from a macro-sized particle, the material will be composed of multiple magnetic domains. As the size is reduced, the particles will reach a critical radius size (r_c) where it is energetically favorable to maintain only one magnetic domain, shown in Figure 1.7. These are referred to as single-domain particles. At this critical size (r_c), there is no conflicting moments due to the presence of other domains, and the surface-to-volume ratio is still low enough that the surface spins do not drastically affect the magnetic properties. The r_c is dependent upon the exchange energy and anisotropy energy of the material and spherical particles near or at this size can achieve their maximum coercivity. Assuming the particle shape remains isotropic, as the size is decreased below r_c the particles become more susceptible to thermal energy and the coercivity will begin to decrease. For many materials, the particles will reach a size, denoted as the superparamagnetic radius r_{sp} in Figure 1.7, where the thermal energy is enough to overcome the anisotropy energy, and it reaches the superparamagnetic state. The r_{sp} can be calculated from

$$r_{sp} = \left(\frac{6k_BT}{K}\right)^{1/3} \quad 1.27$$

where *K* is the magnetocrystalline anisotropy.[13] From eq 1.27 it is easy to see that materials with higher magnetocrystalline anisotropy will reach the superparamagnetic state at smaller sizes. It is important to note that when the particles are not spherical, shape anisotropy can contribute to the total magnetic anisotropy, which will be discussed in section 1.3.2, and influence the superparamagnetic limit.

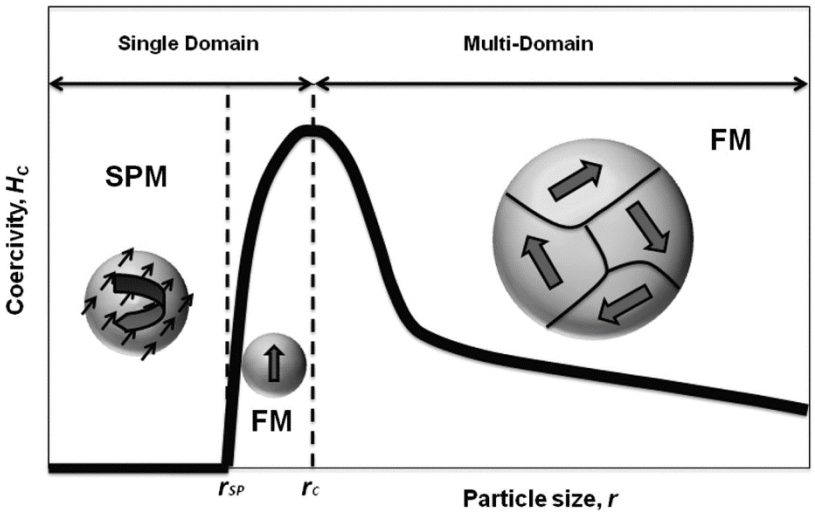

Figure 1.7 An overview of the effects of particle diameter size on the magnetic behavior of a ferromagnetic material. FM refers to ferromagnetic and SPM refers to superparamagnetic.[13]

Although the general case involves the decrease of coercivity with decreasing size of nanoparticles below r_c, surface effects become more prominent as the surface area to volume ratio increases and can have significant effects on the magnetic properties of some magnetic materials. This is most often seen for spinel structured magnetic ferrites, where the magnetic properties of the surface spins are strongly related to the coordination symmetry of the oxygen and metal ions in the tetrahedral and octahedral sites. At the surface, there is a higher concentration of defects (e.g. missing oxygen atoms) that reduce the coordination symmetry and lead to more anisotropic magnetic properties compared to the core properties.[14]

1.3.2 Shape Anisotropy

The effects of shape on magnetic nanomaterials is strongly related to the demagnetizing fields H_d produced in an anisotropic material. The magnetic field lines that travel from the north pole to the south pole of the magnet will generate a field H_d, that opposes the interior magnetization direction, illustrated in Figure 1.8, and is proportional to the magnetization so that

$$H_d = N_d M \tag{1.28}$$

where N_d is the demagnetizing factor.[3] The demagnetization factor N_d can be decomposed into three components, one for each axis of the particle, whose sum will only have a single value that can be calculated if the shape of the particle is an ellipsoid. In SI, it is expressed as a sum so that

$$N_d = N_a + N_b + N_c = 1 \tag{1.29}$$

where N_a, N_b, and N_c, are the demagnetization factors along the a, b, and c axes, respectively.[3] For a sphere, since all axes are equal, all components of the demagnetization factor will be equal and therefor will not have any shape anisotropy. Apart from the sphere, there are two other general shapes to consider, the prolate spheroid (cigar shape) and the oblate spheroid whose demagnetizing factors were calculated by E. C. Stoner and J. A. Osborn.[15,16] For the prolate spheroid,

$$N_c = \frac{1}{(x^2-1)}\left[\frac{x}{\sqrt{x^2-1}}\ln\left(x+\sqrt{x^2-1}\right)-1\right] \tag{1.30}$$

$$N_a = N_b = \frac{1-N_c}{2} \tag{1.31}$$

where x = c/a, often referred to as the aspect ratio. It can be inferred from equations 1.30 and 1.31 that as the aspect ratio increases, the demagnetizing factor along the c-axis decreases whereas the other two increase. Therefor the magnetization becomes more stable along the c-axis.

For the oblate spheroid

$$N_b = N_c = \frac{1}{2(x^2-1)}\left[\frac{x^2}{\sqrt{x^2-1}}\arcsin\left(\frac{\sqrt{x^2-1}}{x}\right) - 1\right] \quad 1.32$$

$$N_a = 1 - 2N_c \quad 1.33$$

In this case, as the aspect ratio increases, N_b and N_c decrease while N_a increases. In addition to the magnetocrystalline anisotropy, the shape anisotropy will also contribute to the total magnetic energy, which can be expressed as

$$E_{sh} = \frac{1}{2}\mu_0(N_a - N_c)sin^2\theta = K_s sin^2\theta \quad 1.34$$

where E_{sh} is the energy due to shape anisotropy, θ is the angle between the c axis and the magnetization direction, and K_s is the shape anisotropy constant.[3]

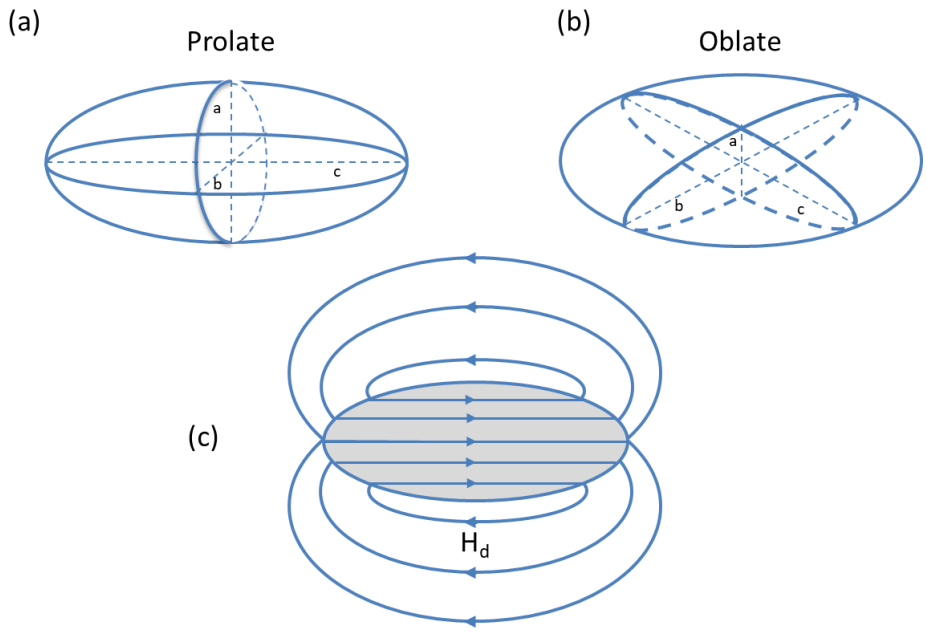

Figure 1.8 Example shapes for (a) a prolate spheroid and (b) oblate spheroid. (c) Example of demagnetization field lines of a magnetized ellipsoid.

1.3.3 Stoner-Wohlfarth Model

In 1947, E. C. Stoner and E. P. Wohlfarth proposed a model to explain the mechanism of magnetization motion of a single-domain ferromagnetic material, which provided important insight into their magnetic properties.[17] It is assumed that the moments in a single-domain ferromagnetic material remain parallel to one another as the magnetization is rotated away from the easy axis by an applied field, demonstrated in Figure 1.9. This mode of rotation is known as coherent rotation. The final direction of magnetization in this mode of rotation is the result of the competition between the anisotropy energy and magnetostatic energy. As the applied field forces the direction of magnetization to rotate, the anisotropy energy opposes the rotation so that it lies between the applied field and initial magnetized direction. For simplicity, the particle is assumed to be a noninteracting ellipsoid that is magnetized along the easy axis, parallel to the c axis. Since the anisotropy energy can come from multiple sources (mainly the shape and crystal), a constant known as the effective anisotropy constant K_{eff} is defined as the sum of the anisotropy constants from each source so that the total anisotropy energy of a uniaxial particle can be expressed as

$$E_a = K_{eff} sin^2\theta \tag{1.35}$$

where θ is the angle between the c axis and the magnetization direction. The magnetostatic energy is expressed as

$$E_m = -H_a M_s \cos(\varphi - \theta) \tag{1.36}$$

where φ is the angle between the c axis and the applied field.[3] The total energy is therefore

$$E = E_a + E_m = K_{eff} sin^2\theta - H_a M_s \cos(\varphi - \theta) \tag{1.37}$$

and the component of magnetization in the field direction is

$$M = M_s \cos(\varphi - \theta). \tag{1.38}$$

which is more conveniently expressed as[3]

$$\frac{M}{M_s} = \cos(\varphi - \theta). \tag{1.39}$$

If the applied field is not in the same direction as the easy axis ($\varphi \neq 0$), the magnetization direction will become unstable and flip to the opposite direction at a critical value of H_a and a corresponding critical angle θ_c. The critical angle is found by solving equation 1.39 for θ so that

$$\tan^3 \theta_c = -\tan \varphi \tag{1.40}$$

whereas the critical field is found by taking the second derivative of equation 1.37 and setting it to zero so that

$$\frac{d^2E}{d\theta^2} = 2K_{eff}(\cos^2 \theta - \sin^2 \theta) + H_a M_s \cos(\varphi - \theta) = 0. \tag{1.41}$$

Using equation 1.25 and substituting θ with θ_c, equation 1.41 can be rearranged so that[3]

$$\frac{H_a}{H_c} = \sqrt{1 - \frac{3}{4}\sin^2 2\theta_c}. \tag{1.42}$$

By plotting M/M_s vs H_a/H_c, the hysteresis loops like those in Figure 1.9 can be predicted for a ferromagnetic single-domain particle.

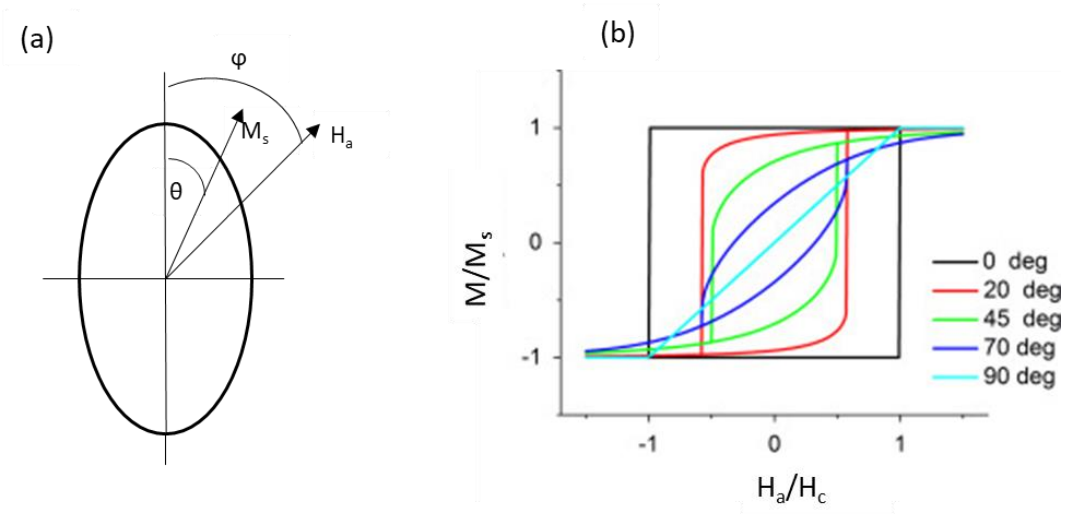

Figure 1.9 (a) An illustration of the magnetization direction under an applied field and (b) the calculated hysteresis loops of the particle for different values of ϕ.[18]

1.3.4 Interparticle Interactions

Up until this point, the properties of nanoparticles have only been considered for non-interacting systems. However, in many cases magnetic nanoparticles will interact with one another through various means that can have significant effects on the properties of the overall nanoparticle system. One of the more prominent interactions is the dipole interaction. The dipole interaction stems from the magnetostatic potential between two magnetic particles and can be present in both ferromagnetic and superparamagnetic systems. If two interacting magnetic particles are considered, the dipole energy potential can be expressed by

$$E_d = \frac{m^2}{r^3}(1 - 3\cos^2\theta) \qquad 1.43$$

where r is the distance between the centers of the two particles, m is the magnetic moment, and θ is the angle between m and r.[2,3] It is immediately seen that this interaction is strongly dependent on interparticle spacing and orientation. Therefore, dilute solutions of nanoparticles will have little

or negligible dipole interactions. However, highly concentrated solutions or assemblies of nanoparticles will have strong dipole interactions that can lead to phenomena such as dipole ferromagnetism. Dipole ferromagnetism occurs when the dipole interactions between particles are strong enough to influence the direction of their moment, which in turn can make it more difficult to rotate their magnetization and lead to an enhanced H_C. The influence of dipole interactions in soft-magnetic materials (e.g. Fe, FeCo, and spinel ferrites) is often investigated by using the Vogel-Fulcher model for spin relaxation

$$\tau = \tau_0 exp\left[\frac{E_a}{k_B(T-T_0)}\right] \quad 1.44$$

where T_0 is the dipolar coupling strength, also known as the Vogel-Fulcher temperature.[19]

Apart from dipole interactions the other major interaction particles can have with one another is exchange coupling. This particular interaction requires that the particles be in very close proximity, so that the spins from each particle can couple across the interface of the interacting particles. This effect is most often seen in core-shell particles, where a particle of one magnetic material is coated with another, such as the $SmCo_5$/FeCo core shell nanocomposite. However, this effect is also induced for densely packed nanoassemblies. Exchange coupling is of particular interest for developing exchange-coupled hard/soft nanocomposite materials, where the goal is to improve the magnetization of the hard magnetic material with high coercivity and fairly low *Ms* by coupling it to a soft magnetic material that has a high *Ms*.

1.3.5 Overview of Co-based Nanostructured Magnetic Materials

Despite the large selection of ferromagnetic materials that can be made, there is only a few that can be found naturally, the most well-known being iron, cobalt, and nickel. While each of these three elements have been investigated and used in the development of many important

magnetic materials, Co has received considerable interest in the development of nanostructured magnetic materials for a variety of reasons. One of the most important reasons for investigation is the anisotropic features of hcp Co. Even though the hcp phase has a magnetic moment per atom slightly smaller than the fcc phase (1.75 μ_B for fcc and 1.72 μ_B for hcp), the non-cubic structure of the hcp phase presents a much higher magnetocrystalline anisotropy, making it a more magnetically hard material. Aside from the features related to the hcp phase, Co also has strong exchange interactions that originate from its 3d electrons, as well as exhibit strong spin-orbit coupling, which is useful in the development of composite magnetic materials and Co containing compounds.

One of the first uses of Co in the development of magnetic materials was making FeCo soft magnetic alloys. The most striking feature of FeCo as a magnetic material is its incredibly high *Ms* of 245 emu/g (for the composition $Fe_{65}Co_{35}$), which to date is one of the largest M_S experimentally achievable. In addition to its substantial magnetization, FeCo alloys also benefit from having high T_C values (above 1200^o C), making it desirable in high temperature applications. Co also played an important role in the development of permanent magnets, a summary of which is given in Figure 1.10. One of the earliest permanent magnets, the AlNiCo magnet, was developed by T. Mishima in the 1930s and was composed of Fe, Co, Ni, and Al. It presented much higher values of H_C than any of the steel-based magnets of that time, as shown in Figure 1.10.[20] The high H_C is a result of finely dispersed precipitates of FeCo with high shape anisotropy in a Ni-Al matrix. The FeCo precipitates are developed by a heat treatment process (typically around temperatures of 850^o C) where a spontaneous diffusion process known as spinodal decomposition causes the FeCo to separate from the Ni-Al. By applying a magnetic field during this process, the FeCo

precipitates become elongated and align to one direction, allowing the H_C to reach values up to 2.04 kOe (162.3 kA/m).

During the 1960's, Co played an important role in the discovery of rare-earth permanent magnets with predicted energy products higher than 20 MGOe, which is drastically higher than the energy products achieved by the AlNiCo magnets.[21] From this newly discovered family of magnetic materials, $SmCo_5$ quickly became popular due to its ability to obtain incredibly high coercivity values (above 30 kOe) and having a Curie temperature as high as 720° C.[22,23] However, the $SmCo_5$ magnets suffer from relatively low magnetization values and were outclassed by the NdFeB magnets that were developed during the 1980s.

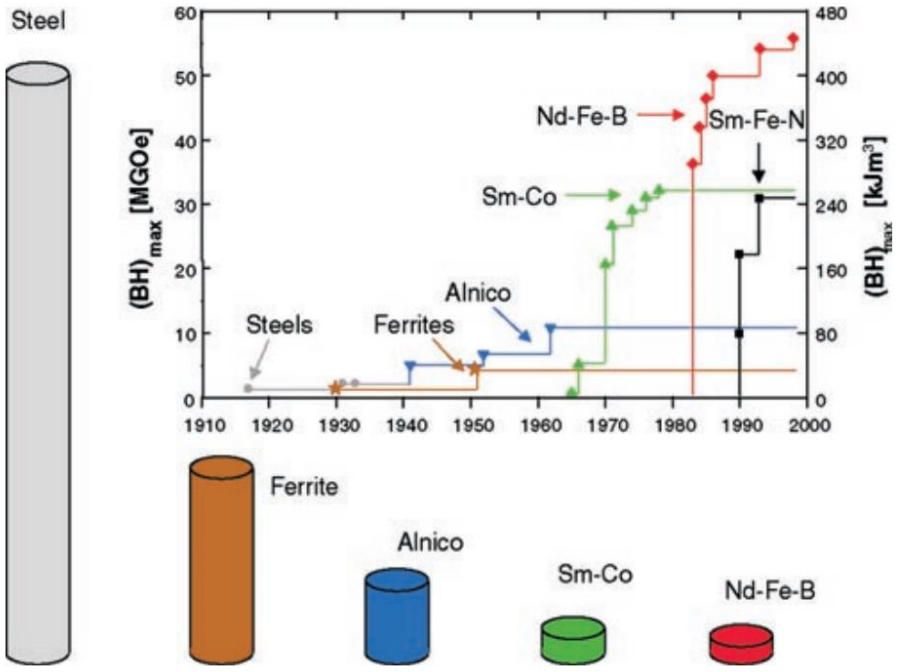

Figure 1.10. The timeline of the development of energy product $(BH)_{max}$ in the most widely used families of permanent magnets.[24]

In more recent years, Co has been extensively used in the development of nanostructured magnetic materials. Co based nanoparticle ferrites were some of the earliest developed

nanostructured magnetic materials and continue to be a popular magnetic material to study for a broad range of potential applications including spintronics, magnetic hyperthermia, and magnetic data storage. Due to the higher magnetocrystalline anisotropy of Co ferrite compared to other ferrites, it has also been used to investigate the effects of alignment in nanoparticle systems. Recently, Tancredi et. al. has shown that aligning Co ferrite nanoparticles with an external field and freezing them in a matrix of 1- octadecene can result in a low temperature coercivity as high as 30.2 kOe, which is higher than any other reported low temperature coercivity for Co ferrite.[25] In addition to the interest in its magnetocrystalline anisotropy, Co ferrite nanoparticles have also recently been investigated for spin glass systems. Studies have shown that Co ferrite nanoparticles have a size dependent relation with spin glass interactions that can lead to increased coercivity at low temperatures.[26]

One of the more prominent areas of interest for Co based magnetic nanostructures is the development of magnetically hard rare-earth-free magnetic nanomaterials via the synthesis of high shape anisotropy nanoparticles. For example, researchers recently developed a technique to produce single crystal and single domain Co nanowires with high coercivity above 12 kOe and $(BH)_{max}$ above 40 MGOe.[27] The considerable improvement in the coercivity and energy product of the hcp Co has made it a potential magnetic material for rare-earth-free permanent magnets. The success of the coercivity enhancement in Co nanowires has also prompted the development of high anisotropy in other materials such as CoNi nanowires and Fe nanorods.

CHAPTER 2 Materials Synthesis and Characterization

2.1 Growth Mechanisms

Understanding the fundamental mechanisms and the factors that influence the growth of nanostructured materials is important in the design of synthesis techniques. While there exists a variety of methods in which nanostructures can be made, several follow similar mechanisms that can be used to describe the growth process. By understanding the mechanisms of growth, the growth of the nanostructures can be controlled to obtain not only particles with specific sizes, but also various shapes that can be tailored for specific applications.

2.1.1 LaMer Theory

The LaMer theory is commonly used to describe the process of nanoparticle formation and growth for many wet-chemical bottom-up approaches. This mechanism considers the concentration of reacted unstable species, which will be referred to as monomers, that are dissolved in solution as a function of time, shown in Figure 2.1. As the reaction proceeds, the monomer concentration builds up in solution, eventually reaching levels of supersaturation. At a critical level of supersaturation, the formation of particles becomes energetically favorable and a burst of nucleation occurs to lower the monomer concentration below the critical supersaturation level. The level of supersaturation needed to initiate nucleation is dependent on multiple factors, which can be seen from the classical description of free energy

$$\Delta G = -RT\ln S + \sigma A \qquad 2.1$$

where R is the gas constant, S is the degree of monomer saturation, σ is the net solution-particle interfacial energy, and A is the particle surface area.[28] After nucleation, the monomer concentration

continues to lower at a slowing rate as they diffuse into the surface of the nucleated particles, typically through a diffusion controlled process. However, during this portion of the reaction smaller particles can re-dissolve into the solution and deposit onto larger particles, known as Ostwald ripening. A mathematical description of this process was given by Lifshitz and Slyozov in 1961.[29] In general, the Ostwald ripening is a result of the higher surface energy of the smaller particles, which leads to a higher solubility and a tendency to re-dissolve, and it is generally avoided as it can lead to polydispersity in the size range of the particles.

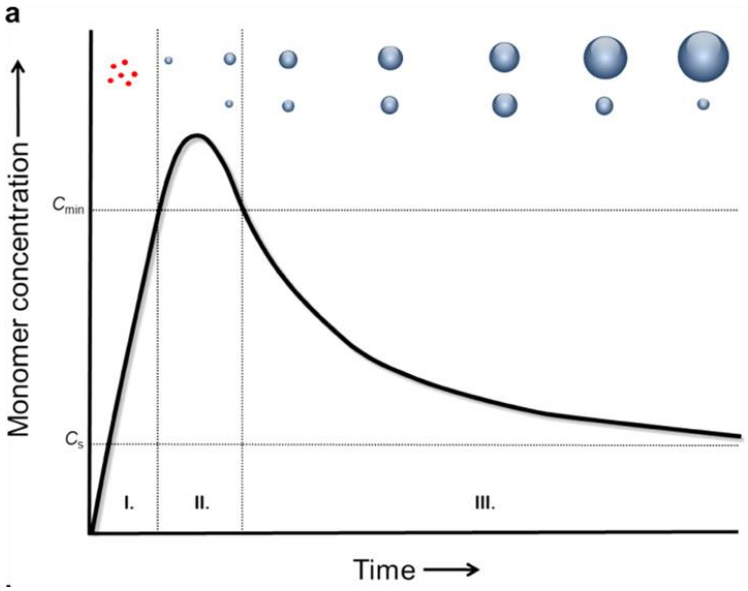

Figure 2.1 General illustration of the Lamer mechanism. Stage I is the build-up of monomers to the supersaturation level (C_{min}). Stage II is the nucleation step that drops the monomer concentration below C_{min}. Stage III is the growth step where the concentration drops until it reaches a point (C_s) where further growth proceeds by Ostwald ripening.[30]

From the LaMer mechanism, techniques have been developed to help promote monodisperse synthesis of nanoparticles, such as the separation of the nucleation and growth

steps.[31,32] By separating the two steps, the growth of particles from existing nucleates can be controlled without the formation of new smaller particles. This is also achieved by using "seeds" of previously prepared nucleates, which are added to a prepared solution so that nucleation of new particles is avoided and only growth takes place.[32,33] Alternatively, the monodispersity can be improved by maintaining the monomer concentration at a constant level in order to prevent Ostwald ripening from occurring.[30]

2.1.2 Anisotropic Growth of Nanoparticles

The overall shape of a nanoparticle is largely determined by the surface energies of the crystal facets, which varies for each crystallographic direction. For example, in Fe_3O_4 the order of surface energy (γ) for each facet is $\gamma 111 < \gamma 100 < \gamma 101$.[34] In general, a crystal that is bound by planes (A_1, A_2, A_3…) will have a total surface energy of [35]

$$\gamma_t = \sum A_i \gamma_i. \qquad 2.2$$

For a crystal at equilibrium, the total energy will be at a minimum. The shape of a crystal can often be predicted by using a Wulff construction, an example of which is shown in Figure 2.2, which minimizes the surface energy for a fixed volume.

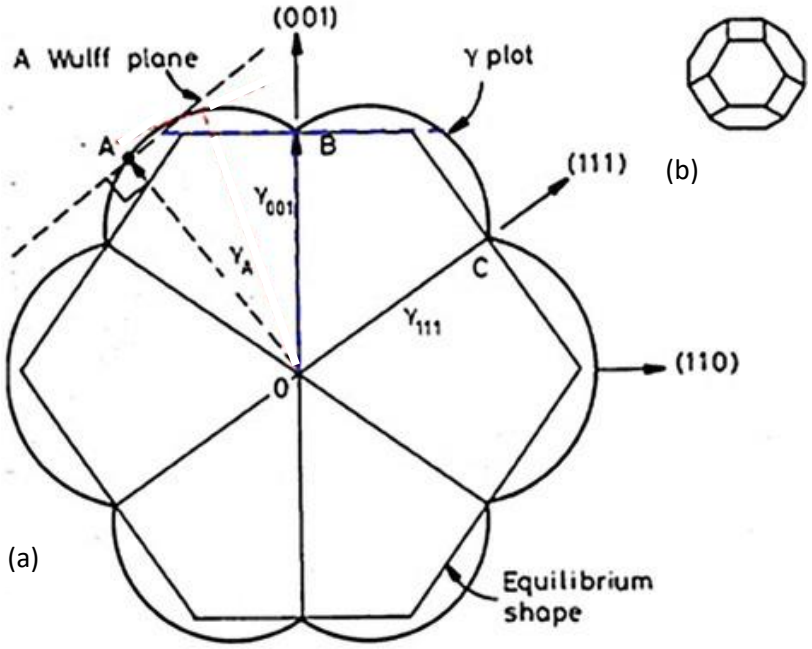

Figure 2.2 (a) A section of a Wulff construction for an fcc crystal viewed from the (-110) side. The surface energy of a plane is represented by a line from the origin to a point on the plot (such as the line OA), which lies in the same direction as the normal to the plane. The planes at the cusps (B, C, etc.) will give the equilibrium shape of the crystal. The inset (b) is the resulting 3D shape. [35]

Although a nanoparticle has a theoretically favorable shape based on the surface energies, there are many other factors that influence the growth that can change its final shape. Surfactants are commonly used in nanoparticle synthesis that bind to the surface of the nanoparticles and they can act as both a capping agent to maintain separation, dispersion, and chemical stability, as well as control the shape of the particles during synthesis. Each surfactant has a specific binding energy, which can create a preference to which facet the molecule will attach to. This can in turn reduce the growth rate of the facets that the surfactants bind to, allowing various shapes including rods, cubes, octahedral etc. to be synthesized.[34,36,37] For the case of hcp Co nanorods, hexadecylamine

(HDA) has a preference for the lateral facets of the crystal structure, which promotes growth along the (0001) direction. However, in a separate study hcp Co nanodisks were obtained when using a combination of alkyl amines and TOPO.[38] The temperature during the reaction can also have a significant role in the shape of a crystal. Returning to the example of Fe_3O_4, slower heating rates allow for more equal growth of all the facets of an Fe_3O_4 crystal, leading to a more spherical shape.[34] However, a faster heating rate leads to a more preferential growth along the (001) and (101) facets, which results in an octahedral shaped particle with (111) facets.

2.2 Synthesis Methods

The synthesis of nanostructured materials is itself not a trivial area of research. Although there are methods and materials that appear to have a simple process, many of the difficulties lie in the ability to obtain nanostructures with precisely controlled shapes, sizes, and compositions. This can be crucial in many applications such as hyperthermia cancer treatments, where the heating properties of the nanoparticles are dependent on their size, shape, composition, and structure.[39] The complexity of the process can vary by the technique, precursors, or even heating rate. Small changes in any of the parameters can have considerable effects on the final outcome of the product, and precise control over the reaction is necessary in order to obtain desired nanoparticles. As such there are several developed techniques, each with their own benefits and shortcomings.

In a more general sense, there are two approaches to making nanomaterials, from the top-down or bottom-up. The top-down approach starts from a bulk material and is processed into smaller pieces, either chemically or mechanically, until nano-sized particles are obtained, and it is generally cheap and able to be used to make large quantities. In contrary, the bottom-up approach builds particles from atoms or molecules and is generally more effective at controlling the shape,

size, and structure of the nanomaterial. In this work, we focus more on techniques that use the bottom-up approach.

2.2.1 Thermal Decomposition

The thermal decomposition method is a relatively direct process that involves the reduction of a chemical by heating it to a high enough temperature to break the atomic bonds in the chemical. It is commonly used to produce metallic, metal oxide, and carbon nanoparticles.[40,41] Depending on the precursors used, this type of reaction can require high temperatures which necessitates a high boiling solvent for wet-chemical methods. Commonly used solvents include (but are not limited to) oleylamine, 1-octadecene, and benzyl ether. However, the need for higher temperatures can make it difficult to obtain particles with a specific crystal phase or shape. To avoid this, compounds with low decomposition temperatures are often used. In the synthesis of Co nanoparticles via thermal decomposition, researchers have used compounds such as cobalt acetate and cobalt carbonyl for their relatively low decomposition temperatures.[42] In the investigation of Co nanowire assemblies in Chapter 4, a thermal decomposition method is used to produce nanowires on a large scale using the setup in Figure 2.3.

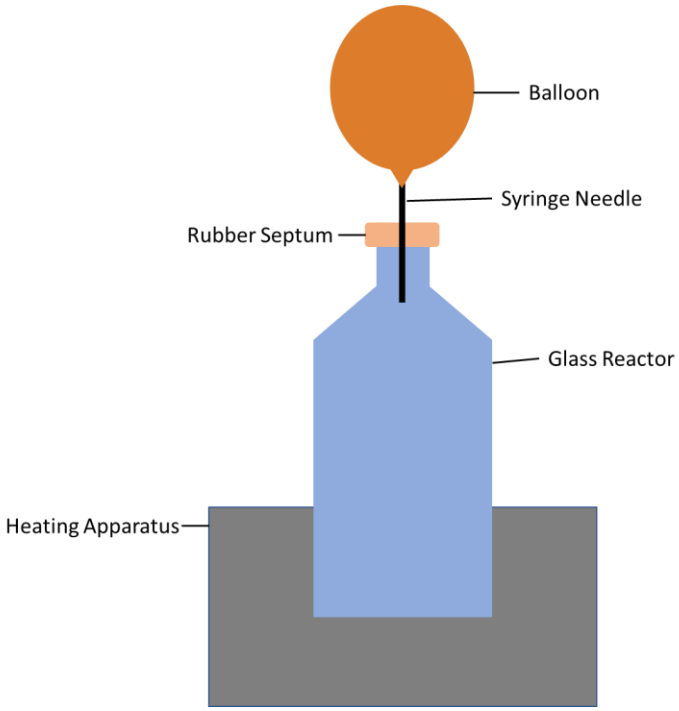

Figure 2.3 The schematic of the glass reactor setup used in the large-scale thermal decomposition reaction.

The solvothermal reaction is a modified thermal decomposition method and is popular for producing semiconductor, metallic, and oxide nanoparticles with high crystallinity and well controlled shapes and sizes. In a typical reaction, the precursors and solvent are placed in a reaction vessel, typically a Teflon lined steel autoclave, capable of withstanding high pressure and high temperatures. In the high-pressure environment, the solvent can be heated beyond its boiling temperature and allow higher solubility. In some cases, this method is used with water as a solvent and is called a hydrothermal reaction. In a hydrothermal reaction, the water can reach a supercritical state at which the dielectric constant can vary across a large range and cause drastic changes in solubility.[43]

2.2.2 Polyol Based Reaction

The polyol method is a robust wet-chemical process that uses a polyol as the solvent, reducing agent, and even surfactant for the synthesis of nanoparticles with well controlled shapes, sizes, and crystallinity. In a typical polyol reaction, a diol such as ethylene glycol and its derivatives are used in the reduction of a metal salt, such as metal chlorides, hydroxides, or acetates. The relatively high dielectric constant of the polyol allows for many different types of inorganic metal precursors to be dissolved, so that it first acts as the solvent before reducing the metal precursors.[44] Additionally, polyols can have boiling temperatures above 300^{o} C so that high temperature reduction can occur without the need for a high-pressure container. Due to the presence of several OH groups in the polyol molecule, it also has coordinating properties that allow absorption to the surface of metallic and oxide nanoparticles, preventing agglomeration and allowing stable colloidal dispersions.[45] In some cases, an intermediate solid phase forms before final reduction, as in the case of reducing $Co(OH)_2$ and $Ni(OH)_2$ into their respective metallic phases.[30] It has also been used in the synthesis of other cobalt-based metal and metal oxide nanoparticles including CoNi, CoO, and Co carbide nanoparticles.[46-48]

2.2.3 Precipitation/Coprecipitation

Precipitation and coprecipitation methods are often favorable methods of producing metallic nanoparticles due to their straightforward procedures, low temperature requirements, and low-cost chemicals. In the synthesis of metallic nanoparticles with this method, typically, metal salts are dissolved into an aqueous solution and a strong reducing agent (such as sodium borohydride, sodium hydroxide, or hydrazine) is introduced to rapidly reduce the metal salts. A surfactant, such as citric acid, is also often used to prevent the immediate oxidation and agglomeration of the metallic particles. Metallic nanoparticles composed of Co, Fe, and Ni are often prepared using this method.[49-51] However, due to the rapid reduction and precipitation of the

metal ions this method can often result in amorphous metallic nanoparticles, which can have reduced magnetic properties from the poor crystal ordering.[52]

2.3 Characterization Techniques and Related Physics

While there exists multiple techniques to explore the properties of a material, in this work the focus will be kept to the techniques used in the presented work. In the investigation of nanostructured materials, there are multiple important areas of characterization, including: crystal structure, morphology, and magnetic properties. X-ray diffraction (XRD), Mossbauer spectroscopy, and transmission electron microscopy (TEM) are used for the determination of crystal structure and composition. TEM and scanning electron microscopy (SEM) are widely used in nanostructure imaging. For magnetic properties, the vibrating sample magnetometer (VSM), alternating gradient magnetometer (AGM), superconducting quantum interference device (SQUID), and physical property measurement device (PPMS) are the more common devices used.

2.3.1 X-ray Diffraction

First demonstrated in 1912 by German physicist von Laue, when x-rays are passed through a crystalline material, they can interact with the atoms and result in a diffraction pattern. The patterns are a result of the wave-like nature of the X-rays and the periodic arrangement of atoms in a crystalline material. The X-rays have wavelengths around the same order as atom spacing (~1 Å) so that they are able to pass through and scatter off the atoms. As they scatter, the X-rays can undergo constructive interference or destructive interference. In constructive interference, the wave vectors of the X-rays are in phase so that their periods match and can be considered a single electromagnetic wave with an amplitude equal to all of the constituent amplitudes combined. In

destructive interference, the waves are not in phase, and the overall amplitude is reduced. In general, the conditions for constructive or destructive interference is described by Bragg's Law

$$n\lambda = 2d \sin\theta \qquad 2.3$$

where n is an integer, λ is the X-ray wavelength, d is the interplanar spacing between two adjacent and identical crystal planes, and θ is the angle of incidence between the X-ray and crystal plane.[53] In an XRD device, the wavelength of the X-rays is usually kept constant so that constructive or destructive interference is dependent only on the crystal nature of the material and the angle of the X-rays. Since the interplanar spacing of a family of planes is unique to the crystalline material, the angles at which constructive interference occurs will be unique to that material.

One of the most common methods of XRD is the powder diffraction method, where a sample in the form of a fine powder is used so that all possible diffraction directions are possible to detect. As the angle of the incident X-rays and X-ray detector are rotated, the intensity of diffracted X-rays is measured to obtain Bragg peaks. The angle at which the peaks occur, and their intensity are used to determine the crystal structure of the material. The resolution of the peaks is strongly related to the angle increments the machine is capable of rotating. Smaller angles will provide more clear peaks and help distinguish between peaks located near one another. In the presented work, the Rigaku Ultima IV is used for XRD measurements with a minimum step of 0.0001 (0.0002 for 2θ) degrees. A Cu K_α (X-ray wavelength of 1.54056 Å) element was used as an X-ray source. Samples are typically prepared by drop casting a concentrated dispersion of nanoparticles onto a glass slide and allowed to dry.

2.3.2 Scanning Electron Microscopy

The SEM is a type of electron microscope that uses a beam of focused accelerated electrons to scan the surface of a sample. As the electrons interact with the sample, a variety of signals are produced, including secondary electrons (SE), backscattered electrons (BSE), and X-rays. The most common imaging mode uses the SE, which are electrons that have been ejected from the sample through inelastic collisions between the beam electrons and electrons in the atoms of the sample. The intensity of the SE is measured for a given spot, so that an image is formed from the collected distribution of intensities for each spot of the scanned area. The resolution of the SEM is dependent upon the beam size, which is controlled by the operating voltage and focusing magnetic lens, and most modern SEM have resolutions in the range 1-20 nm. In this work, the Hitachi S-4800 II FE SEM was used to obtain sample images at operating voltages 0.5-30 keV. The samples are prepared by drop casting a dispersion of the nanoparticles, using either toluene or chloroform as a solvent, onto a copper or silicon substrate. The samples were then placed in a vacuum to ensure they were completely dried. For aligned assemblies, high concentrated solutions are used, and the samples are dried under and external field generated by an electromagnet.

2.3.3 Transmission Electron Microscopy

The TEM is a more powerful electron microscope capable of obtaining images with atomic-scale resolution, allowing for not only well-defined morphology features, but also information on the crystal structure. The TEM works off the principle described by de Broglie, where the wavelength of an object is related to its mass (m) and velocity (v)

$$\lambda = \frac{h}{mv}$$

where h is the Planck constant. The wavelength of an electron can be made small enough to pass through the crystal lattice to obtain high resolution images. To obtain information regarding the

crystal structure of the sample, the TEM can be operated in a diffraction mode to obtain selected area electron diffraction (SAED) patterns. The Hitachi H-9500 High-resolution transmission electron (HR-TEM) microscopy operated at an accelerated voltage of 300 kV with a resolution of 1.8 Å was used to obtain images of the samples presented. Samples are prepared by drop casting dilute dispersions onto a carbon coated copper grid and dried in atmospheric conditions. The samples are then kept in vacuum to dry completely.

2.3.4 Vibrating Sample Magnetometer

The VSM is a straight-forward method of measuring the magnetic properties of a material based on the *emf* of a changing magnetic field near a copper coil. In a VSM, the magnetic sample is mounted to the end of a nonmagnetic rod that is attached to a mechanical vibrator. The sample is then oscillated between a pair of coils under an applied field, which generates an *emf* that is proportional to the magnetic moment of the sample as follows

$$emf = \beta M \cos \omega t$$

where β is a constant, ω is the frequency of oscillation, and t is the time.[54]

The VSM is very versatile and can be operated at high or low temperatures, given the proper adaptations. Its capable of reaching fields as high as 140 kOe (14 T) and can detect magnetic moments down to 10^{-5} emu (10^{-8} Am^{-2}). Often times, it is integrated into a SQUID, which will be discussed below, as a faster measurement option. The majority of hysteresis loops and magnetic measurements in this work are done using a physical property measurement system (Quantum Design Dyanacool-PPMS) equipped with the VSM. As-prepared samples were measured using a fine powder of the samples that were dried without any control over the atmospheric conditions or use of external fields. Aligned assemblies were prepared in the same way as the SEM samples.

2.3.5 Alternating Gradient Magnetometer

The AGM is similar to the VSM in that the sample oscillates between a pair of coils. However, instead of using mechanical vibration to produce an *emf*, the coils produce an alternating gradient magnetic field to generate a force that oscillates the magnetic sample. The rod holding the sample is attached to a piezoelectric fiber that produces a voltage proportional to the amplitude of the oscillation, which in turn is related to the magnetic moment of the sample. This method is capable of measuring magnet moments as low as 10^{-6} emu (10^{-9} Am^{-2}), however, it is limited to small samples due to the mass dependency of the vibration amplitude and cannot perform measurements at high or low temperatures. The Princeton Measurements Corporation Alternating Gradient Magnetometer is used to obtain minor hysteresis loops of samples in this work. As-prepared samples were measured by taking a small amount of sample powder and wrapped it in Teflon before loading onto the sample stage.

2.3.6 Superconducting Quantum Interference Device

The SQUID design is based on the change in magnetic field lines in a given area, known as magnetic flux $\Phi = BA$, as the sample is extracted from a search coil. The change in flux as the sample is extracted from the search coils will generate a current that is converted to a voltage by the connected SQUID sensor. The variations in the voltage are proportional to the moment of the sample and obtains accurate measurements of the magnetization. The high sensitivity is maintained by using a superconducting shield to hold a constant magnetic field during the measurement. The sensitivity of the SQUID can be as high as 10^{-7} emu (10-^{10} $Am\text{-}^{2}$) which is an order higher than the AGM and can operate between 2 and 400 K, however, it is a much slower process compared to the AGM. Additionally, the SQUID requires liquid helium to operate, making it more expensive.

2.4 Error and Uncertainty

Despite the level of precision modern characterization machines can achieve, there is always a level of uncertainty involved with any measurement. In most cases, the uncertainty is primarily determined by the characterization machine and the prepared sample being measured. The uncertainty from the machine is limited to the maximum precision it can achieve. To help reduce any other uncertainties that may be involved with the machine, it is often calibrated by measuring a well-known substance with well-defined properties. Additionally, multiple measurements are taken for samples to calculate the standard deviation, which is used to establish the possible range of error in a measured sample. Any uncertainty that originates from the sample primarily occurs from the preparation. For example, SEM can obtain images on the scale of 1 nm, however, it requires the sample to be metallic and the presence of organic substances (i.e. surfactants) can drastically reduce the resolution. In magnetic measurements, the presence of surfactants will also affect the magnetization values of the sample and must be accounted for when determining the true magnetization value.

CHAPTER 3 Magnetic Properties of $CoFe_2O_4$ and $FeCo/CoFe_2O_4$ Nanoparticle Assemblies

3.1 Introduction

Magnetic ferrite nanoparticles have attracted increasing attention due to their remarkable size and shape dependent magnetic properties which allow them to fulfill a wide range of applications such as in ferrite-based batteries, targeted drug delivery, diagnostics, and gas sensing.[55,56] In particular, magnetic nanoparticle assemblies (MNPAs) with periodic arrangements and tunable spacing are important for many applications such as spintronics, magnetic data storage, and nanoparticle-based bonded magnets. The most unique feature of the MNPAs is that they exhibit tunable collective properties that are different from the sum of their constituents. The magnetic response of a nanoparticle assembly is due to a combination of finite-size and surface effects, and cooperative behaviors owing to inter/intra-particle interactions.[57,58] The finite-size and surface effects become pronounced as the nanoparticle size decreases. The reduced symmetry of surface atoms, due to the broken exchange bonds, results in high surface anisotropy and consequently an enhanced effective magnetic anisotropy with complex magnetic phenomenon like surface spin-glass and exchange bias.[19] More importantly, the magnetic properties of ferrite compounds are governed by an antiferromagnetic super-exchange interaction between metal cations mediated by an intervening oxygen ion. Because of the indirect nature of the coupling, the surface effect is always pronounced in ferrite nanoparticles.[59,60] On the other hand, when the size of the nanoparticles is large enough, a sufficient portion of the spins have bulk coordination, exhibiting magnetization and effective magnetic anisotropy comparable to their bulk materials. The presence of interparticle interactions, namely the dipole-dipole interactions between neighboring nanoparticles (due to high magnetization) and the exchange interactions between the

magnetic spins at the surface of neighboring nanoparticles in contact, plays a key role in the magnetic properties of nanoparticle assemblies.[61-64] These magnetic interactions can give rise to collective disordered and ordered magnetic states known as super spin-glass, dipolar ferromagnetism, and superferromagnetic states.[65] $CoFe_2O_4$ is an especially interesting ferrite because it possesses higher magnetic anisotropy and coercivity compared to the other spinel ferrites due to the strong spin-orbit coupling from the Co^{2+} cation. In particular, certain magnetic behaviors arise when the particle size is decreased to sub-10 nm size, and the surface spin-disorder effects become non-negligible.

In this work, we explore the role of surface spin disorder on the magnetic properties of two groups of $CoFe_2O_4$ nanoparticles with average sizes of 3.5 nm and 16 nm, respectively. Additionally, an alternative approach is used to modulate the magnetic coupling between the nanoparticles through the enhancement of intrinsic magnetic properties (magnetization and magnetocrystalline anisotropy) via fabrication of exchange-coupled core-shell nanoparticles, in which the magnetization of the $CoFe_2O_4$ is improved by addition of a high magnetization FeCo soft phase and later assembled into nanoparticle superstructures. Successful formation of the elongated arrays with hcp ordering leads to an enhanced magnetic coercivity and a collective spin-glass-like relaxation process as confirmed by the magnetometry measurements.

3.2 Experimental Methods

$CoFe_2O_4$ nanoparticles were synthesized using a previously published protocol.[66] In a typical synthesis of 3.5 nm $CoFe_2O_4$ nanoparticles, 4 mmol of iron (III) acetylacetonate, 2 mmol of cobalt (III) acetylacetonate and 10 ml of benzylamine were taken in a European style three-neck round bottom flask. The reaction solution was heated to 120 °C with continuous flow of N_2 gas and kept at this temperature for 15 min. The temperature was then elevated to 240 °C at a heating

rate of 5 °C min^{-1} for 2 h. The obtained black colored precipitate was centrifuged and washed with a mixture of hexane and ethanol several times. The 16 nm $CoFe_2O_4$ nanoparticles were synthesized by using 24 mmol oleylamine instead of benzylamine. To measure the magnetic properties, the $CoFe_2O_4$ nanoparticles were dispersed in toluene with a concentration of ~ 20 mg/ml and then dried in a petri dish. The obtained three-dimensional assemblies of nanoparticles were taken for magnetic measurements.

Monodisperse FeCo/$CoFe_2O_4$ core-shell nanoparticles were produced via a thermal decomposition process. In a typical reaction, iron (III) acetylacetonate (1 mmol), cobalt (III) acetylacetonate (1 mmol), 1,2-hexadecanediol (10 mmol), oleic acid (6 mmol), oleylamine (6 mmol), and benzyl ether (20 mL) were mixed in a European flask using a mechanical stirrer. The reaction mixture was refluxed at a temperature of 300 °C for 2 hours with a continuous flow of 7 % hydrogen balance argon gas. After synthesis, the black color precipitate was separated by centrifugation and washed several times with hexane and acetone. The nanoparticles were then dried and dispersed in toluene for the assembly preparation.

Mesocrystals of the FeCo/$CoFe_2O_4$ core-shell nanoparticles were prepared by evaporating the toluene dispersion of nanoparticles (10 mg/ml) onto a Si substrate placed in a glass vial. The evaporation rate of toluene was controlled by keeping the glass vial on a water-cooled aluminum block. After the solvent evaporated completely, the nanoparticle assembly was transferred to a vacuum oven for further drying and then taken for structural and magnetic measurements. To grow large aligned mesocrystals, the glass vial containing nanoparticles dispersion and Si substrate was kept and allowed to dry under the external magnetic field of 1.0 T in an electromagnet.

To confirm the crystal structure and morphology of the prepared $CoFe_2O_4$ nanoparticles, the X-ray diffraction (XRD) patterns were collected from a Rigaku Ultima IV diffractometer with Cu

K_α X-ray source and high-resolution transmission electron microscopy images were obtained with Hitachi H-9500 operated at an accelerated voltage of 300 kV. The magnetic properties of the nanoparticle assemblies were studied using a physical property measurement system (Quantum Design Dynacool-PPMS). The zero-field-cooled (ZFC), and field-cooled (FC) magnetization were measured over the temperature range 10–400 K with an applied field of 50 Oe to 5 kOe. The field dependent magnetization curves were measured with an applied magnetic field of 90 kOe. The training effect of exchange bias was measured at 5 K under field cooling in 90 kOe from 300 K. The thermoremanent magnetization (TRM) measurement was done by cooling the sample from 300 K to 10 K in an external magnetic field of 100 Oe, then the field was turned off and the magnetization was measured upon warmup.

The structural properties of $FeCo/CoFe_2O_4$ core-shell nanoparticles and their assemblies were measured using a Rigaku Ultima IV diffractometer with a Cu K_α X-ray source, a 120 kV JEOL 1200 EX transmission electron microscopy (TEM), a Hitachi S-4800 ultra-high-resolution scanning electron microscope (FE-SEM) and a Perkin-Elmer Phi 560 X-ray photoelectron spectroscopy (XPS). To confirm the oxidation state of Fe and Co in the prepared samples, room temperature 57Fe Mössbauer spectroscopy was measured. A Mössbauer spectrometer (SEE Co. Minneapolis, MN USA) was calibrated against α-Fe foil. The magnetic properties of the samples were studied using a physical property measurement system (Quantum Design Dynacool-PPMS). The zero-field-cooled (ZFC), and field-cooled (FC) magnetization were measured over the temperature range 10–400 K with an applied field of 50 Oe. The frequency dispersion of the AC susceptibility (f = 11, 111, 1111, and 9999 Hz; amplitude 5 Oe) was measured as a function of temperature.

3.3 Surface Effects on Magnetic Properties of $CoFe_2O_4$ Nanoparticle Assemblies

3.3.1 Morphology and Structural Characterization

Figure 3.1a and 3.1b show the transmission electron microscopy (TEM) micrographs of $CoFe_2O_4$ nanoparticles synthesized by following a previously reported synthesis approach.[66] The average particle size estimated using a lognormal distribution are 3.5 nm and 16 nm. Figure 1c shows the X-ray diffraction patterns of $CoFe_2O_4$ nanoparticles with average sizes of 3.5 nm and 16 nm. All the diffraction peaks are indexed to the $CoFe_2O_4$ phase with spinel cubic crystal structure (ICDD 022-1806). We can see that the diffraction peaks of 3.5 nm $CoFe_2O_4$ nanoparticles are very broad, a further indication that the grain size is small.

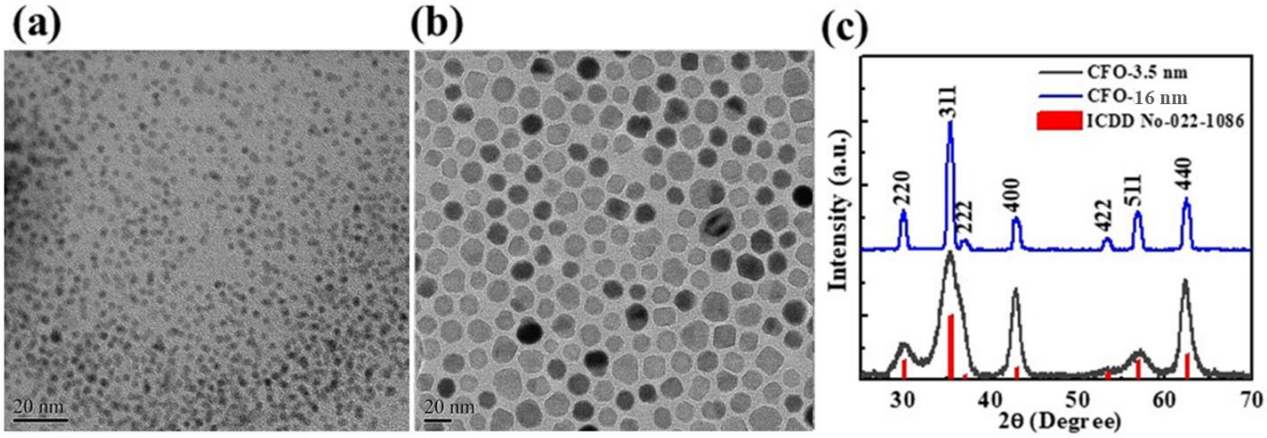

Figure 3.1 TEM micrographs of $CoFe_2O_4$ nanoparticles: (a) 3.5 nm and (b) 16 nm. (c) The corresponding XRD patterns of the $CoFe_2O_4$ nanoparticles.

3.3.2 Magnetic Hysteresis Characterization

To confirm the effect of surface anisotropy on the magnetic properties of $CoFe_2O_4$ nanoparticles, the magnetic hysteresis loops are measured at the temperature of 300 K and 5 K. Figure 3.2a shows the hysteresis loops of the 3.5 nm sample. The magnetization value at 90 kOe is found to be ~ 30 emu/g, which is nearly one third of the bulk value (80 emu/g).[3] In ferrite nanoparticles, it is common to have low magnetization with smaller sizes because of the disordered surface spins. The surface-spin-disorder layer thickness can be calculated by using the formula $M_S = M_{Bulk}[1 - (6\,t/d)]$, where *d* and *t* are nanoparticle size and spin-disorder layer thickness, respectively.[56] The calculated spin-disorder layer thickness for 3.5 nm $CoFe_2O_4$ nanoparticles is around 0.4 nm. In addition, the sample is magnetically very hard, and the magnetization is far from the saturation at a field of 9 T. More importantly, the sample is exhibiting an exchange bias up to 2.8 kOe and training behavior due to the strong pinning occurring at the spin-frustrated interface of the ferromagnetic ordered core (see Figure 3.2b). The observed exchange bias and training behavior is in good agreement with the results obtained for γ-Fe_2O_3 nanoparticles.[67] In addition, Figure 3.2b shows a prominent exchange bias shift, which signals the close relationship between the ferromagnetic core with high anisotropy and the freezing of the surface spin glass. Our interpretation is that the open hysteresis loop at high field is the result of irreversible changes between the surface spin configuration rather than reversal of magnetization of the nanoparticles. Further, the large irreversibility in the high field is a characteristic of surface spin-glass which is induced by the frustrated spin structure on the surface and large surface anisotropic field.[58,68] In contrast, the 16 nm sized $CoFe_2O_4$ nanoparticles show typical ferromagnetic behavior with a saturation magnetization value of 80 emu/g (Figure 3.2c). The high saturation magnetization indicates less surface spin-disorder effects in the 16 nm $CoFe_2O_4$ nanoparticles. Despite having an

ordered structure, the coercivity of the 16 nm $CoFe_2O_4$ nanoparticles at 5 K (~19 kOe) is less than that of the 3.5 nm sized nanoparticles (~23 kOe). This further supports the fact that the ultra-small sized $CoFe_2O_4$ nanoparticles are magnetically harder than the larger sized $CoFe_2O_4$ nanoparticles. The enhanced coercivity can be attributed to the high magnetic field required for the switching of the spins that are pinned by the exchange interactions with the frozen surface spins.[69]

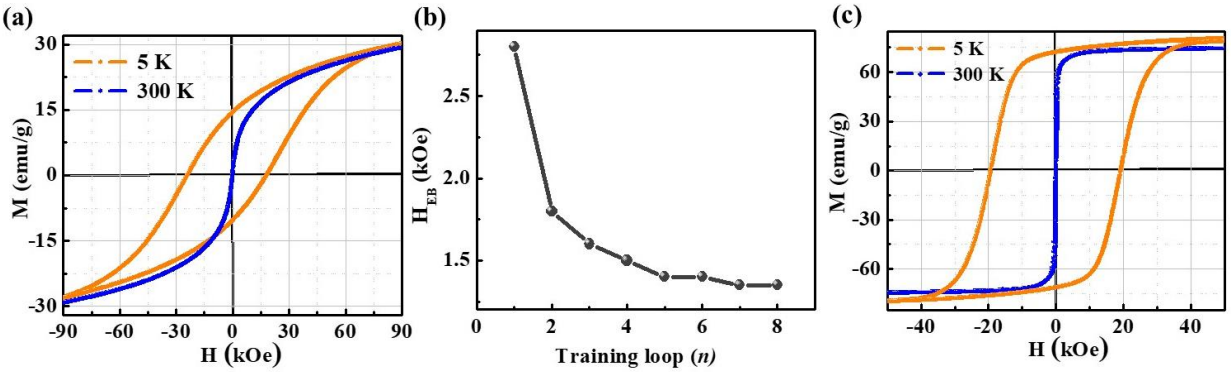

Figure 3.2 (a) Hysteresis loops measured at 300 K and 5 K, and (b) dependence of exchange bias field (H_{EB}) on the number of magnetic hysteresis cycles, measured at 5 K after field cooling in 90 kOe for 3.5 nm $CoFe_2O_4$ nanoparticles. (c) Hysteresis loops measured at 300 K and 5 K for 16 nm $CoFe_2O_4$ nanoparticles.

3.3.3 Zero-Field-Cooled and Field-Cooled Characterization

Figure 3.3 represents the variation of magnetization with temperature, measured under different applied fields in the zero-field-cooled (ZFC) and field-cooled- (FC) protocols. The peak temperature of the ZFC magnetization curves for 3.5 nm and 16 nm $CoFe_2O_4$ nanoparticles measured under 50 Oe field occurs at 90 K and 398 K, respectively (see Figure 3.3a and 3.3c). This peak is conventionally taken as the blocking temperature T_B associated with

superparamagnetic nanoparticles. The field dependency of the T_B in both samples show two different trends. The T_B in 3.5 nm sized $CoFe_2O_4$ nanoparticles increases with the increase of the applied magnetic field, while that for the 16 nm sized $CoFe_2O_4$ nanoparticles strongly decreases with the increase of applied magnetic field. In the former case, the blocking temperature shifts from a low temperature to a high temperature, which implies the presence of an exchange coupling between the surface disordered spins and the core spins. A similar behavior has been theoretically predicted by Lee et. al.[70] Further, the observed exchange bias effect in Figure 3.2a agrees with the blocking temperature behavior of 3.5 nm sized $CoFe_2O_4$ nanoparticles. In contrast, the 16 nm $CoFe_2O_4$ nanoparticles show an opposite trend of T_B with the applied magnetic field. The T_B strongly decreases from 398 K to 230 K with increasing magnetic field from 50 Oe to 5 kOe. The sharp decrease of blocking temperature is a mimic of the spin-glass behavior. The flat nature of the FC curve observed at temperature around 250 K further confirms the presence of spin-glass-like state in the 16 nm $CoFe_2O_4$ nanoparticles. More importantly, the blocking temperature of both samples measured at the low field of 50 Oe is higher than the corresponding theoretical blocking temperatures (25 K for 3.5 nm and 308 K for 16 nm $CoFe_2O_4$ nanoparticles). The enhanced blocking temperature is attributed to the intraparticle and interparticle interactions.

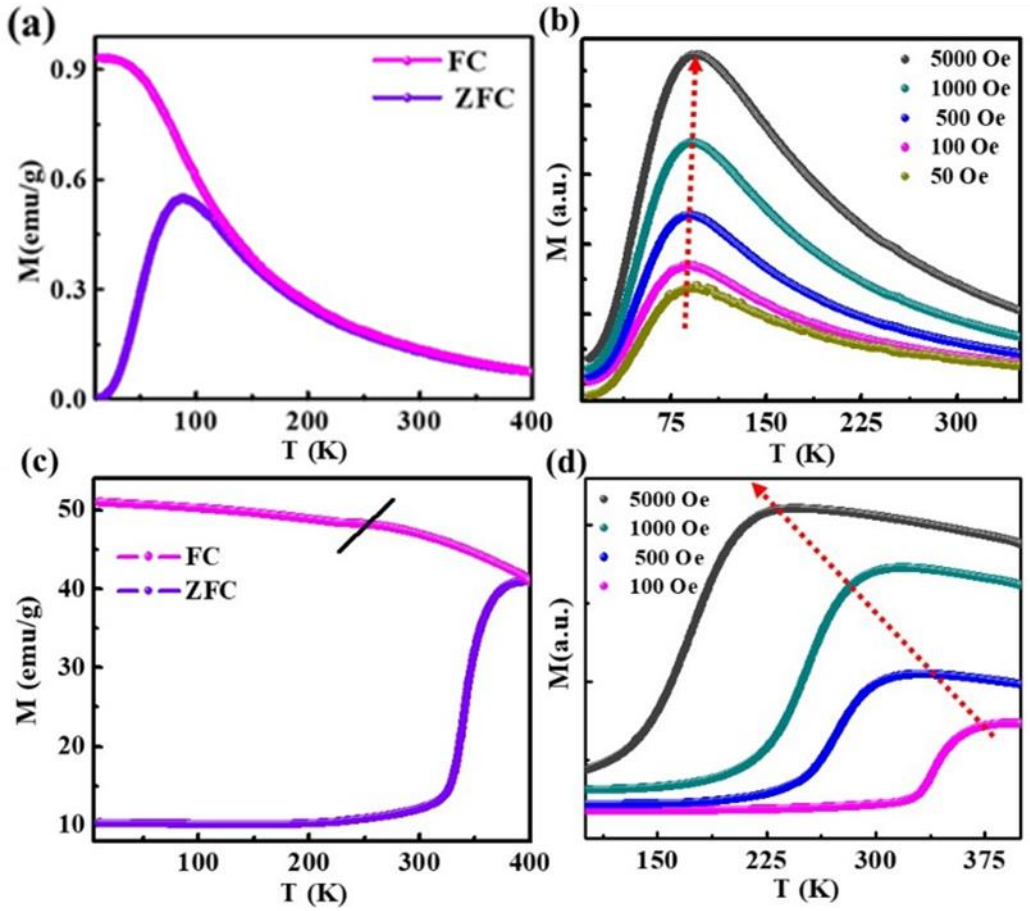

Figure 3.3 Temperature dependence of ZFC-FC magnetization measured in 100 Oe applied magnetic field and the ZFC magnetizations measured at the indicated field values for (a, b) 3.5 nm and (c, d) 16 nm $CoFe_2O_4$ nanoparticles, respectively.

When comparing the magnetic properties of both the samples, we can consider the nanoparticles as a core-shell model. The core refers to the inner part of the nanoparticles that exhibits bulk-like magnetic ordering whereas the shell layer refers to a spin-disorder surface. In larger sized nanoparticles (in our case 16 nm), the surface spin disorder effect is minimized and thus particles exhibit high magnetization values and consequently strong interparticle interactions. The strong magnetic interparticle interactions within the nanoparticle assembly lead to quasi-

magnetostatic states like super spin-glass. As the particle size decreases, the magnetic properties of the surface layer become more important due to the growing surface-to-volume ratio. At the lower temperature, the spins in the disordered shell begin to create magnetically ordered clusters when they interact with the applied magnetic field. The subsequent growth of the ferromagnetic region in the shell, aligned in the field direction, allows for exchange coupling with the ferromagnetic core of the nanoparticle, making its reversal more difficult, and thus strongly enhancing the effective anisotropy of the whole nanoparticle. This enhancement in the magnetic order in the ultra-small sized nanoparticles is evident by the increase of the FC magnetization at low temperatures and the high coercivity at 5 K.

3.3.4 Magnetic Memory Effects

The collective magnetic behavior of the 16 nm $CoFe_2O_4$ nanoparticles is further understood by measuring the thermoremanent magnetization (M_{TRM}) curves with and without a stop at the temperature of 150 K, just below the super spin-glass transition temperature. In a typical measurement, the sample was cooled in a magnetic field of 100 Oe to 10 K and the remanent magnetization was measured upon heating in zero field. To record the memory properties, the sample was cooled again with an applied field of 100 Oe, but this time with a temporary stop at 150 K for a waiting time of 1 h.[71] The comparison of both the remanent magnetization curves (inset of Figure 3.4) indicates that the magnetization relaxed during the temporary stop at 150 K, as can be seen from the step-like features. As the temperature increases continuously, the magnetization recovers the previous M_{TRM} curve at a temperature of 335 K. The decreased magnetization in the memory curve is a typical magnetization relaxation, which happens during the waiting time as the magnetic moment configuration spontaneously rearranges toward equilibrium spin structures. The presence of memory effect and comparative low magnetization in

the memory curve confirm that the nanoparticles are strongly coupled and form a super spin-glass state. A similar memory behavior has been seen in the strongly interacting FeCo and Fe_3N nanocrystalline systems.[72,73] The super spin-glass behavior can be ascribed to the frustration induced due to the randomness in nanoparticle positions and anisotropy-axis orientations.

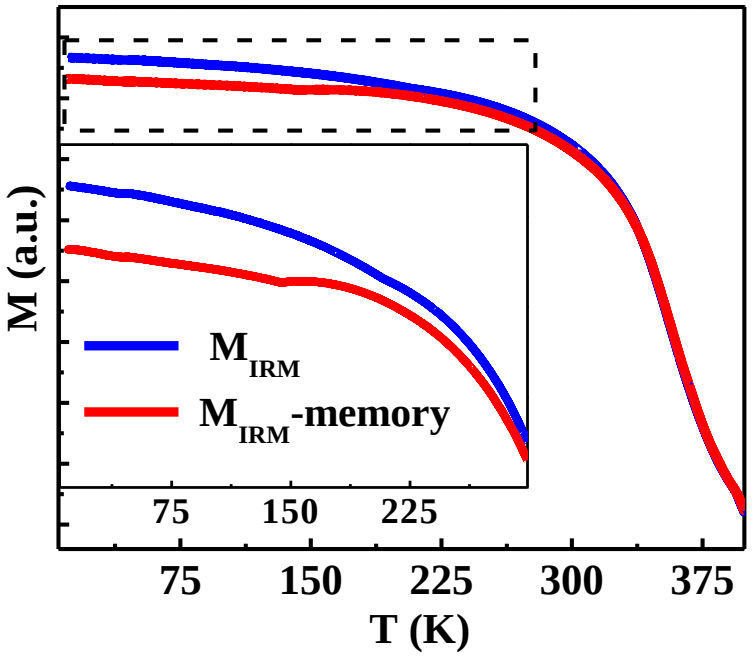

Figure 3.4. Memory effect in the isothermal remanent magnetization curve of 16 nm $CoFe_2O_4$ nanoparticles.

3.4 Structural and Magnetic Properties of FeCo/$CoFe_2O_4$ Nanoparticle Assemblies

3.4.1 Morphology and Structural Characterization

Figure 3.5a shows the XRD pattern of as-synthesized FeCo/$CoFe_2O_4$ nanoparticles. All diffraction peaks of the 20–70° scan could be indexed as the synthesized $CoFe_2O_4$, illustrating a cubic inverse spinel structure (ICDD card no. 022-1086) accompanied by a diffraction peak for

the FeCo (110) plane at a diffraction angle of 45° (ICDD card no. 049-1567). The presence of diffraction peaks of both $CoFe_2O_4$ and FeCo phases confirms the formation of a nanocomposite system. For further confirmation of the nanocomposite formation, the X-ray photoelectron spectroscopy (XPS) spectrum is recorded. The Fe and Co spectrum from as-prepared nanoparticles are shown in Figures 3.5b and 3.5c, respectively. The two characteristic peaks at 711.0 and 724.1 eV in Figure 3.5b are attributed to the Fe^{3+} 2p3/2 and Fe^{3+} 2p1/2 in the $CoFe_2O_4$ phase, respectively. In addition, two extra peaks at 706.7 eV and 721 eV are presented, which are ascribed to $Fe^0$2p3/2 and $Fe^0$2p1/2 in the FeCo phase. At the same time, the Co 2p core-level spectrum (Figure 3.5d) consist of Co 2p3/2 and Co 2p1/2 peaks, which are both fitted with three constituents in regard of Co(0), Co(II), and the satellite peak. The appearance of Fe(0) and Co(0) in the XPS analysis manifests that the nanoparticles are made of $CoFe_2O_4$ and FeCo phases, rather than a pure $CoFe_2O_4$ structure as previously reported.

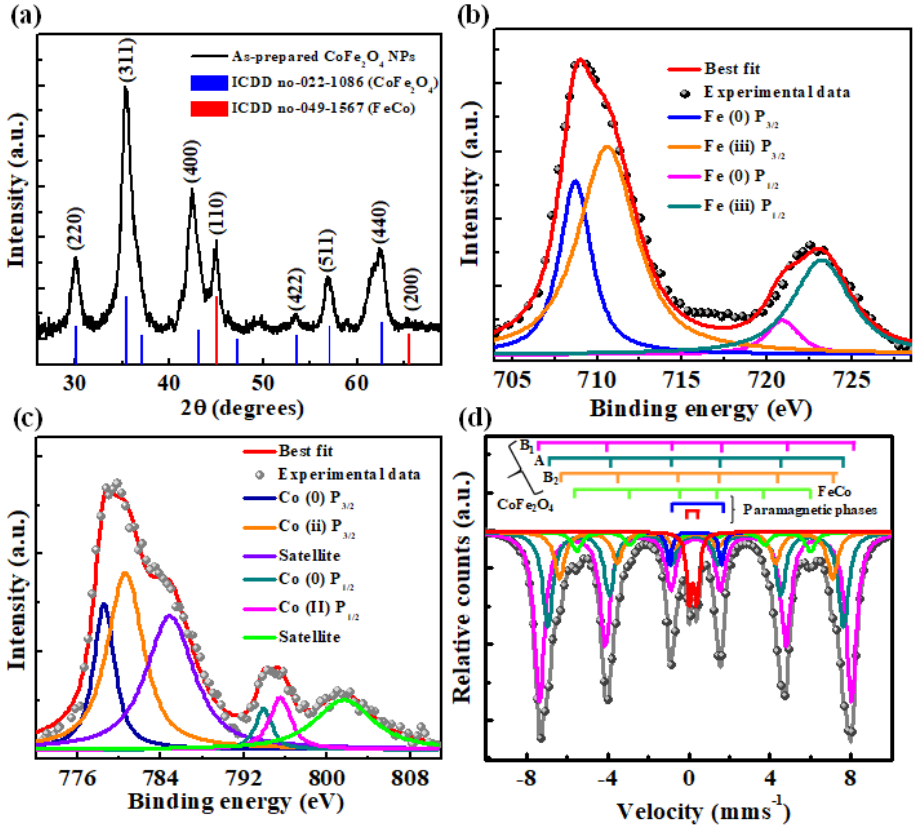

Figure 3.5 (a) XRD patterns of the as-synthesized FeCo/$CoFe_2O_4$ core-shell nanoparticles. The XRD patterns of FeCo and $CoFe_2O_4$ are labeled with respect to standard ICDD cards. (b and c) The XPS spectra of Fe- and Co- spectrum from as-prepared FeCo/$CoFe_2O_4$ core-shell nanoparticles. (d) 57Fe Mössbauer spectra of the FeCo/$CoFe_2O_4$ core-shell nanoparticles recorded at room temperature.

Mössbauer spectrometry was used to determine the oxidation state of Fe and Co in as-prepared nanoparticles. The observed spectrum is fitted with four sextets. A sextet is related to Fe^{3+} in the octahedral (site A) and two sextets to tetrahedral (site B) sites of the $CoFe_2O_4$. While the 4th intense sextet is attributed to the crystalline phase of bcc-FeCo. Additionally, two doublets are added to account for the paramagnetic phases in the as-prepared nanoparticles. Usually the

doublets are assigned to Fe^{3+} and Fe^{4+} occupying octahedral sites in the perovskite phase, respectively. Central doublets also originate from superparamagnetism. It should be noted that an acceptable data fitting was obtained only when the B-site pattern was assumed to be a superposition of more than one sextet. In our case the hyperfine interaction of the B-site was fitted by up to two overlapping sextets, which is in agreement with the reported Mossbauer study on ferrites. This phenomenon is attributed to the random occupancy of the tetrahedral site by Fe^{3+} and Co^{2+} cations.

The transmission electron microscopy (TEM) image shown in Figure 3.6a revealed that the as-synthesized nanoparticles are spherical in shape and monodisperse with an average size of 10.5 nm. Moreover, the nanoparticles are self-organized into a hexagonal assembly with a uniform spacing in between. The reason for such ordered organization is attributed to the binding of long chain oleic acid and oleylamine moieties on the surface of nanoparticles which prevented agglomeration among nanoparticles.

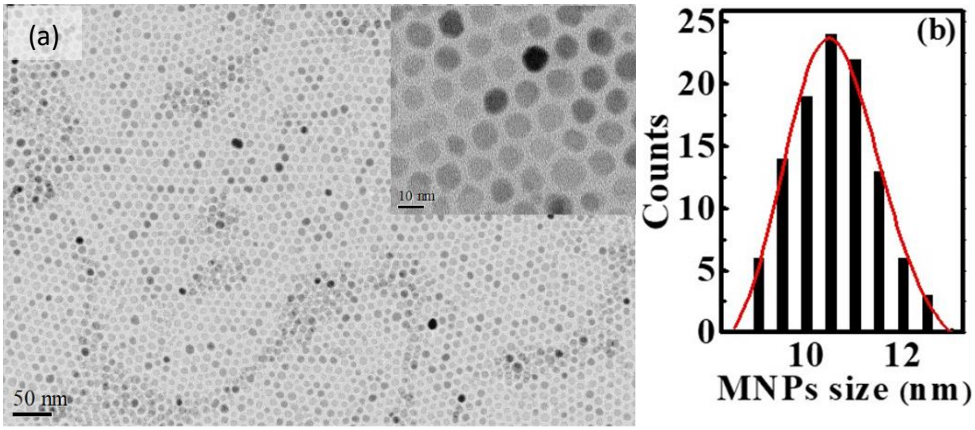

Figure 3.6 (a) TEM image of $FeCo/CoFe_2O_4$ core-shell nanoparticle assemblies prepared via the solvent evaporation techniques. Inset shows high resolution TEM image of the $FeCo/CoFe_2O_4$ nanoparticles. (b) Histogram of the nanoparticle size distribution.

3.4.2 Assembly Formation and Characterization

To investigate the ability of the $CoFe_2O_4$ nanoparticles to form ordered 3D arrays, samples were prepared using the evaporation self-assembly method and a field-assisted assembly method using toluene as a solvent and silicon substrates. As seen in Figure 3.7, the evaporation self-assembly led to long range ordering composed of sub-micron superstructures. However, the field-induced assembly resulted in elongated arrays with cracks propagating along the direction of the magnetic field, shown in Figure 3.7c. In an evaporation self-assembly process, the particle assembly and crack formation are primarily governed by the capillary pressure that arises when the solvent flows from a higher solvent content region to a lower content region near the drying front. The capillary pressure is a negative pressure and helps compact the particles into assemblies, but at the same time there is an in-plane stress that builds up between the substrate/assembly interface as the assembly compacts that will lead to the formation of cracks.[74] Because the particles are superparamagnetic, the application of an external field induces dipolar interactions (discussed in section 1.3.4) amongst the particles, which in turn will influence the way the particles assemble.

As the solvent evaporates and the particle concentration increases, the interparticle spacing is reduced and the dipole interactions become more prominent. Additionally, because the blocking temperature of the particles is near room temperature the particles will attempt to align their magnetic easy axis in the same direction of the applied field, further influencing the assembly process. It is likely that the applied field induces an attracting force between the particles parallel to the field, so that as the solvent dries and the stress between the film and substrate builds up, the cracks are more likely to form and propagate where the particles have less attractive force.

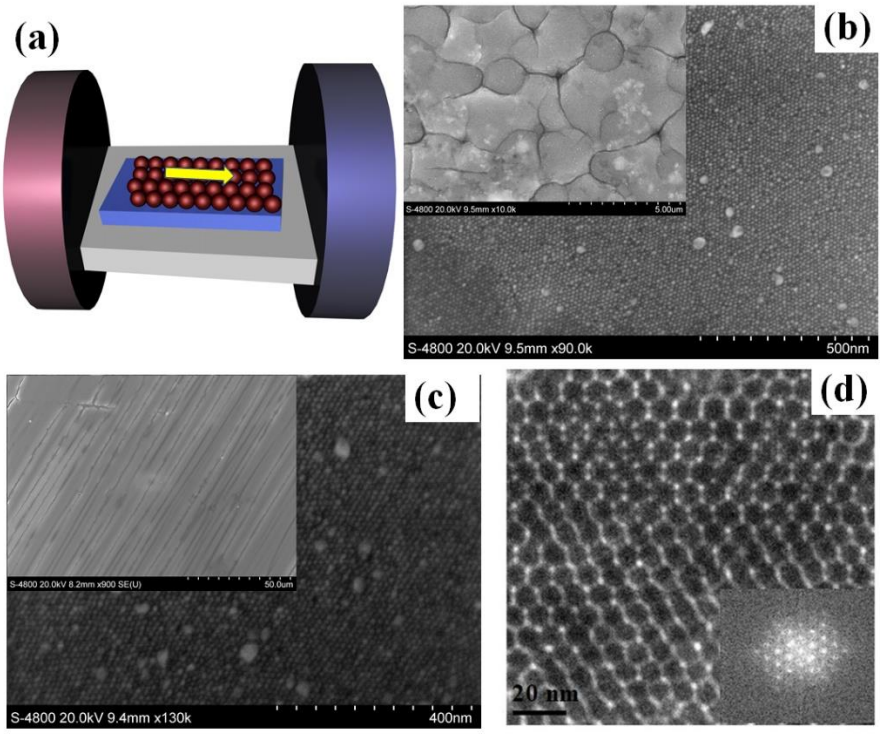

Figure 3.7 (a) Schematic illustration of the experimental setup of magnetic-field-assisted assembly of the FeCo/$CoFe_2O_4$ core-shell nanoparticles. SEM images of the assembled structures prepared with FeCo/$CoFe_2O_4$ core-shell nanoparticles: (b) without magnetic field and (c) under magnetic field. Low magnification SEM image in the inset of (c) reveals the formation of anisotropic superstructures. (d) HRTEM and FFT pattern (inset) of the aligned assembly revealing the hexagonal packing of the nanoparticles.

3.4.3 Magnetic Hysteresis Characterization

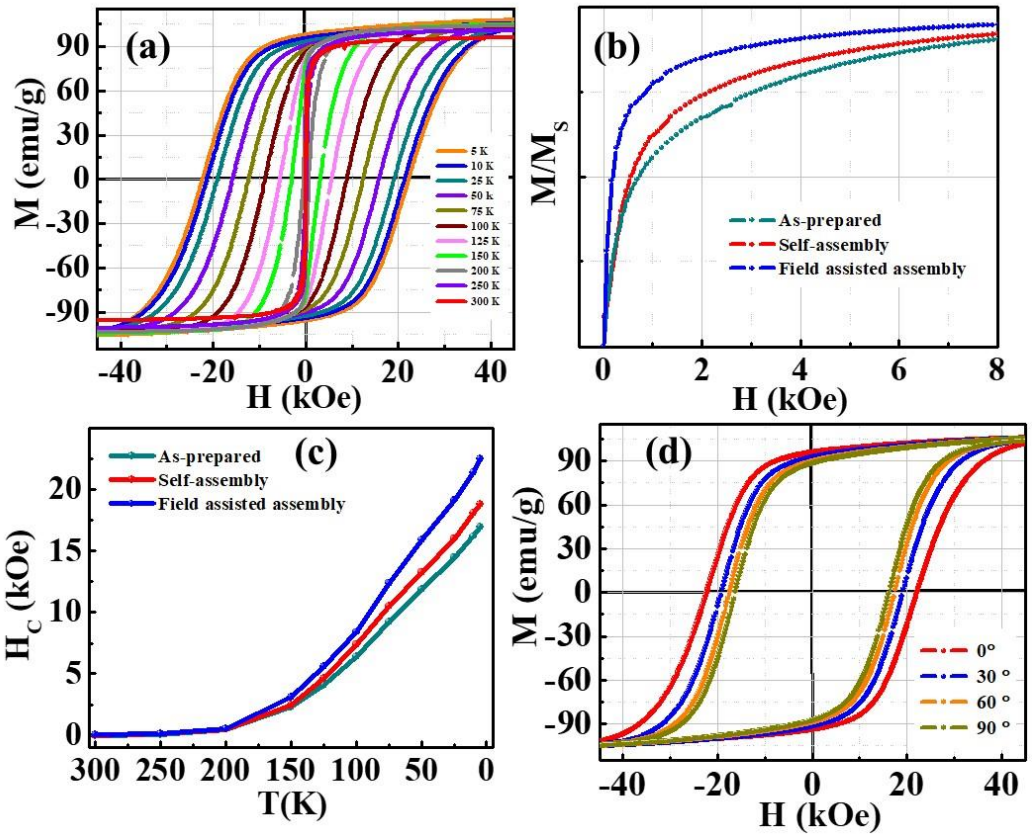

Figure 3.8. (a) Hysteresis loops of the field-assisted nanoparticle assembly at different temperatures. (b) Comparison of the magnetization response to applied field for all three samples. (c) Comparison of coercivity with respect to temperature for all three samples. (d) Angular dependence plot for the field-assisted assembly.

Field- and temperature-dependent magnetic measurements were performed for the as-prepared samples. At 300 K, the magnetization loop shows zero remanence and zero coercivity, indicating that those particles are in the superparamagnetic state with thermally unstable magnetization. The obtained saturation magnetization (M_S) values at 10 K and 300 K are 108 emu/g and 93 emu/g, respectively, which is even higher than the value for bulk $CoFe_2O_4$ materials

(80 emu/g at room temperature).[3] The enhanced M_S is due to the presence of metallic FeCo inside the particles.

To investigate the effects of the assembly on the magnetic properties of the samples, hysteresis loops were measured at different temperatures. Although the coercivities are not distinguishable at room temperature, at lower temperatures the thermal instability is reduced and the coercivity enhancement is much more prominent. In particular, Figure 3.8a shows how the coercivity increased for the field-assisted sample, which is then compared to the coercivity trend of the other samples in Figure 3.8c, showing that the field-assisted assembly and self-assembly had higher coercivity than the as-prepared, with the field-assisted displaying the largest increase in coercivity with a maximum of 22.4 kOe at 10 K. Additionally, Figure 3.8b is a plot of the magnetization ratio as a function of applied field at room temperature which shows that the magnetization of the field-assisted assembly and self-assembly has a sharper more square curve than the as-prepared sample, indicating that the susceptibility is increased when the particles are in an assembly. The considerable increase in the coercivity and magnetic susceptibility for the field-assisted and self- assemblies are attributed to an increase in interparticle interactions. The exchange interactions are more prevalent because the self-assembled nanoparticles have less spacing, causing the magnetic spins in each nanoparticle to interact with other particles more effectively, which increases the susceptibility of the assembly.

It has also been shown that the dipolar interactions in an assembly of magnetic particles can lead to ferromagnet behavior, which can lead to an additional increase in the coercivity of the assembly, as evidenced by Figure 3.8c. Because these particles have a higher magnetization than normal $CoFe_2O_4$, the induced dipolar fields will be stronger and affect a larger range of particles, helping to order their magnetic moments. However, the field-assisted assembly has a much higher

susceptibility and coercivity, which can be attributed to the magnetic anisotropy of the particles. $CoFe_2O_4$ particles have a comparatively higher magnetocrystalline anisotropy than other ferrites, so that the particles have improved magnetic properties along their easy axis. When the particles are assembled under the external magnetic field, they orient their easy axis along the direction of the magnetic field, resulting in considerably higher susceptibility and coercivity along the field direction.[75] This is verified by Figure 3.8d, where the field-assisted assembly is measured at different angles with respect to the assembly alignment direction. The coercivity drops significantly as the measurement field direction is rotated from 0˚ to 90˚ with respect to the aligned direction, further supporting the significant improvement in coercivity due to easy axis alignment. Additionally, the overall shape of the assembly can also influence the anisotropic behavior through shape anisotropy effects, specifically columnar structures will have better magnetic properties when the particles are aligned along the long axis.

3.4.4 Temperature Dependent Magnetization and Susceptibility

The ZFC-FC curves were then taken and compared for the three samples in Figure 3.9a. In the ZFC curve, the magnetic spins are initially fixed in random positions leading to the low magnetic moment. As the temperature is increased, the thermal agitation will help the spins rotate to the easy axis and provides an increase in magnetic moment up to the blocking temperature, where the thermal agitation will then prevent the spins from remaining fixed and decrease the moment. From Figure 3.9a, it is seen that the evaporation self-assembly sample has a slightly higher blocking temperature and magnetic moment, primarily as a result of the exchange interactions of the close-packed particles requiring more energy to become disordered. The field-assisted assembly has an even higher blocking temperature (315 K) and magnetic moment, but more interestingly, it has a sharper peak than the other two samples. Since the easy axis of the

particles are aligned in one direction, as the thermal energy pushes the spins into the easy axis the dipolar interactions help influence nearby spins and lead to a faster alignment of the assembly. Once aligned, the dipolar interactions also help prevent the spins from disordering, leading to the higher blocking temperature and magnetic moment of the field-assisted assembly.

The temperature dependencies of the in-phase ($\chi'(T, f)$) and the out-of-phase ($\chi''(T, f)$) components of the AC magnetic susceptibility for aligned FeCo/$CoFe_2O_4$ nanoparticle assembly are shown in Figure 3.9b. The $\chi'(T, f)$ curve for 11 Hz displays a sharp peak at the blocking temperature T_m= 310 K and it is clear from the figure that the peak position is frequency-dependent. With increase of frequency from 11 to 9999 Hz, the peak position shifts from 310 to 356 K (ΔT_m = 46 K). Similar to $\chi'(T,f)$, $\chi''(T,f)$ (inset of Figure 3.9b) also shows a shift in peak position from 240 to 286 K as the frequency 'f' changes from 11 to 9999 Hz. The frequency dependence of the blocking process can be classified by analyzing the relative shift of T_m of $\chi'(T,f)$ per decade of frequency, i.e. $\varphi = \Delta T_m / T_m \, \Delta \log(f)$, where ΔT_m is the difference between T_m measured in the $\Delta \ln(f)$ frequency interval.[76-78] The value of φ represents the strength of interparticle interaction among magnetic nanoparticles and decreases with an increase of interaction strength. For non-interacting nanoparticles, this parameter 'φ' is usually more than 0.13, for nanoparticle based super spin-glasses, the range is $0.005 < \varphi < 0.05$ and for intermediate interactions it is $0.05 < \varphi < 0.13$.[79,80] In our studies, the φ values calculated for $CoFe_2O_4$ nanoparticle assemblies is ~0.04, which is in similar range of that of super spin-glass systems.[80,81]

To gain further insight into the super spin-glass behavior, the variation of T_m with $\ln(\tau)$ is fitted to the Vogel-Fulcher equation (eq. 1.44).[82] The best fit, shown in Figure 3.9c, is achieved for T_0 = 320 K, 294 K and 275 K for the aligned assemblies, self-assemblies and as-prepared nanoparticles, respectively. The characteristic time 'τ_0'obtained from the fitting is two orders

higher than that of spin-glass systems, which is about 10-13 s. The decrease of relaxation time and enhanced T_0 value are ascribed to the exchange coupling strength between nanoparticles, which increased for the aligned nanoparticles assemblies. Although the values of φ (~0.04) are within the range for super spin-glass, Vogel-Fulcher model fitting of AC data indicates the presence of a strong inter-particle interaction between FeCo/$CoFe_2O_4$ nanoparticles. Fitting the data further with a power-law could provide concrete information about the super spin-glass state. The conventional spin-glass power-law for the critical slowing down of the relaxation time is,[77]

$$\tau = \tau_0 \left(\frac{T_m}{T_g} - 1\right)^{-zv} \quad 3.1$$

where τ_0 is the microscopic relaxation time, T_m is the freezing temperature at a specific observation time, T_g is the spin-glass transition temperature and zv is the dynamical exponent, which takes values from 4 to 12 for typical spin-glass systems. The parameters τ_0 and T_g obtained from the best fit are shown in Figure 3.9d. As we go from the as-prepared FeCo/$CoFe_2O_4$ nanoparticles to their aligned assemblies, the characteristic relaxation time 'τ_0' is observed to decrease from 5.6×10^{-9} s to 8.2×10^{-13} s and exponent 'zv' increases from 9 to 11.1. The value of zv is consistent with that of super spin-glass and in agreement with reported values in the literature for super spin-glass systems, involving strong inter-particle interaction.[77,83-85] The increase of zv values from 9 to 11.1 is due to increase in exchange coupling between the nanoparticles, which is enhanced for the aligned assemblies and self-assemblies due to high packing density. The obtained τ_0 and T_g values increase with particle spacing and are similar to τ_0 and T_0 values estimated using the Vogel–Fulcher law.

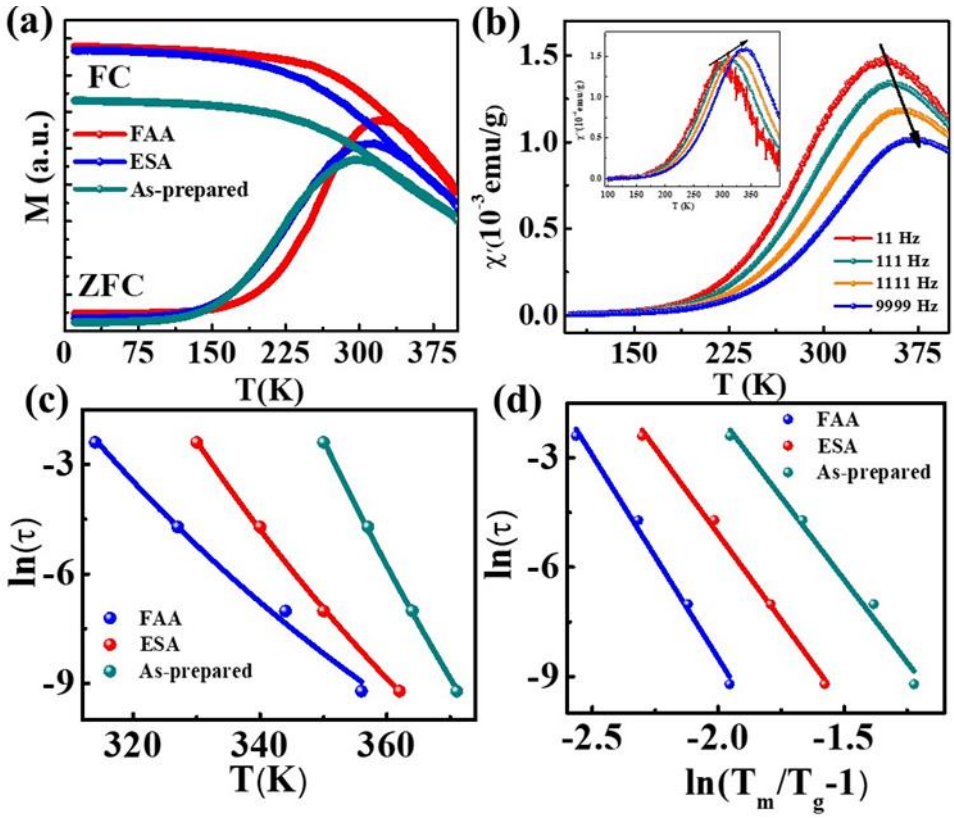

Figure 3.9 (a) Temperature dependence of low field (50 Oe) ZFC–FC magnetization of: as-prepared FeCo/$CoFe_2O_4$ core-shell nanoparticle, their self-assembly and magnetic field-assisted assembly, respectively. (b) Temperature dependence of in-phase ($\chi'(T, f)$) and the out-of-phase ($\chi''(T, f)$) (inset) components of the AC susceptibility for the aligned FeCo/$CoFe_2O_4$ nanoparticle assembly. (c) The frequency dependence of blocking temperature (T_B) of $\chi'(T, f)$ is fitted with Vogel–Fulcher law. (d) The best fit of frequency dependent blocking temperatures (T_m) to the spin-glass power-law, $\tau/\tau_0 = [(T_m - T_g)/T_g]^{-zv}$ for FeCo/$CoFe_2O_4$ nanoparticle assemblies.

3.5 Conclusion

In summary, the effects of surface spin disorder on the magnetic properties of $CoFe_2O_4$ nanoparticles have been investigated by studying structural and magnetic properties of two groups of samples with average size of 3.5 nm and 16 nm. The ultra-small sized nanoparticles exhibit some features similar to surface spin-glass behavior due to prominent surface spin disorder effects, while the larger size nanoparticle assemblies show bulk-like magnetic properties with super spin-glass-like states. The spin-glass-like behavior in 3.5 nm and 16 nm $CoFe_2O_4$ nanoparticles originates from the frustration of the randomly distributed surface spins and the frustration of interparticle interactions that are induced due to randomness in nanoparticle positions and anisotropy axes orientations, respectively. Another noticeable observation is that the 3.5 nm $CoFe_2O_4$ nanoparticles are magnetically hard and exhibit very high coercivity compared to the 16 nm $CoFe_2O_4$ nanoparticles.

FeCo/$CoFe_2O_4$ composite nanoparticles with a high M_S of 108 emu/g were prepared via a thermal decomposition approach and assembled into ordered arrays. The TEM and SEM showed that the particles self-assemble into hexagonal close packed arrays with long range ordering. Both the self-assembly and field-assisted assembly showed enhanced magnetic properties, with a max coercivity of 22.4 kOe at 10 K for the field-assisted assembly. Angular dependence measurements of the field-assisted assembly show that the easy axis alignment of the nanoparticles while assembling can play a significant role in improving the coercivity. Additionally, the blocking temperature is increased from 295 K for the as-prepared to 315 K for the field-assisted assembly. Fitting the AC susceptibility data to the Vogel-Fulcher model confirms the increase of interparticle interactions in the assembled samples, which is due to decreased interparticle spacing. The decreased spacing and increased magnetization also promotes increased dipole-dipole interactions

that can further enhance the magnetic properties. Manipulating the spacing and ordering of these assemblies can have a profound impact on the collective properties of the assembly and is an important consideration for the development of nanoparticle assembly applications.

CHAPTER 4 High Aspect-ratio Co-based Nanowire Assemblies and Their Magnetic Properties

4.1 Introduction

The development of magnetic coercivity in 3*d* metals and their alloys is of paramount importance in advanced magnetic materials technology since they are cheaper compared to rare-earth magnets, and they possess high saturation magnetization (M_S) and high Curie temperature (T_C).[86,87] However, they are known as soft magnetic materials because of their high magnetic susceptibility and low coercivity gained from their low magnetocrytalline anisotropy. A straightforward approach to improve the effective magnetic anisotropy, and consequently the coercivity, can be the control of the shape of nanoscale materials or engineering the crystal structure from a high symmetry cubic lattice to a uniaxial crystal structure to increase K_1 to a sufficiently high value (e.g. FeCo alloys with tetragonal distortion).[88-93] In fact, the use of shape anisotropy to develop coercivity has been confirmed in the early 1930s[20]. The prominent examples of shape anisotropy-based hard magnetic materials are Alnico and Fe-Cr-Co alloys, which contain isolated needles of ferromagnetic FeCo alloys.[94] The shape anisotropy developed from the one-dimensional morphology of FeCo alloys is the main source of coercivity, which otherwise would be a pure soft-magnetic phase. This necessitates reactions that have fine control over the morphology of the particles, which is not a trivial task.

Despite the difficulty of synthesizing 3d nanostructures with high anisotropy, recent experimental work has shown that hcp Co nanowires can reach diameters as low as 8 nm and achieve high values of coercivity of up to 12.5 kOe at room temperature using a solvothermal approach.[95] However, the need for a high pressure reaction vessel makes it difficult to scale up the

reaction for large batches, making this method less favorable for commercial use. Additionally, studies over the potential applications of Co nanowires as a permanent magnet require large amounts of the nanowires to make the magnets. Therefore, it would be beneficial to develop a method that allows for large scale synthesis. Apart from the difficulty of making Co nanowires on a larger scale, Co is used extensively as a catalyst and in batteries, making it less available and more expensive than Fe or Ni and less attractive for commercial use. Unfortunately, many of the Co alloys do not retain the hcp crystal structure even for small additions of a second element. Another approach is to make a nanocomposite of the Co nanowires with a less expensive soft magnetic material such as FeCo. In fact, this has already been done with $SmCo_5$, where the $SmCo_5$ is exchange-coupled with FeCo to improve the magnetization.[96] Herein, we develop and optimize a more suitable approach to synthesize Co nanowires on a larger scale and investigate their magnetic properties in aligned assemblies. Additionally, we use an electroless coating method to coat the Co nanowires with FeCo to improve the magnetization.

The recent advances in the development of high anisotropy Co has also triggered us to consider other 3*d* metals and their alloys into our study. Recently, we have shown improvement in coercivity for FeCo and $Co_{0.8}Ni_{0.2}$ nanowires/nanorods.[97,98] Despite the high shape anisotropy, the Fe-based nanowires/nanorods exhibited low coercivity, which is related to their low magnetocrystalline anisotropy coming from the cubic crystal structure and microstructure imperfections as they prefer polyhedral-shaped growth exclusive to the {111} and {100} type facets.[99] On the other hand, CoNi nanowires have shown high coercivity as they crystalize in the hcp-structure with (0001) as the preferred growth direction.[100] To optimize the magnetic properties of CoNi alloys further, we have controlled their morphology and crystallization process through

variation of the Ni content over a wide concentration range. In addition, the effects of Ni content on the coercivity and energy product are systematically studied.

4.2 Experimental Methods

For the preparation of Co nanowires, 1 g of Co(II) laurate, 6 mg of RuCl3, and 0.2-1.0 g of HDA is added to 15 mL of 1,2 butanediol in a glass reactor. The glass-reactor was purged with forming gas for 5 min then sealed with a rubber stopper. A rubber balloon sealed to a syringe was inserted into the stopper to maintain a small positive pressure with forming gas in the glass reactor. Afterwards, the enclosure was placed in a heated, ultrasonic water bath adjusted to 65°C. The contents within the enclosure were then mixed for 60 min using the ultrasonication. Then, the reaction mixture was placed under 1.2 millibar of forming gas pressure and heated for 15 min at 240 °C. After the reaction, the solution was cooled to room temperature and the obtained black precipitates were washed and centrifuged several times with chloroform. The HDA to $RuCl_3$ ratio was controlled by adjusting the amount of HDA added while keeping the $RuCl_3$ constant. After investigating the effect of HDA concentration on the morphology of the Co nanowires with the small reactor, the reaction volume was increased to a larger scale by using a larger glass reactor, shown in Figure 2.3, while keeping all the precursor ratios constant. Using this setup, nanowires with uniform morphology and coercivity values similar to the 0.8 g HDA small scale reaction were obtained by keeping the same precursor ratios.

The nanowires were coated using an electroless method that has been previously reported.[96] The nanowires were first activated by heating them to 80^{o} C for 1 hr in a solution of sodium hypophosphite dissolved in DI water that has been purged with forming gas. Then, an aqueous solution of Co(II) sulfate, Fe(II) sulfate, ammonium sulfate, and sodium hypophosphite dissolved in DI water was prepared. A solution of sodium hydroxide in water was added dropwise to the

prepared solution to bring the pH to 10. Then, the activated nanowires were added, and the solution was purged with forming gas to remove any oxygen. After sealing the flask, the solution was heated to 80^{o} C for 20 min. After the reaction, the solution was cooled to room temperature and cleaned with ethanol and DI water using a centrifuge.

$Co_{1-x}Ni_x$ bimetallic nanowires/nanoparticles were synthesized using a modified solvothermal method described by previous literature.[95] In a typical reaction, 2 mmol of Ni- and Co-laurates were taken with 4 mmol of hexadecylamine (HDA) and 0.048 mmol of ruthenium chloride ($RuCl_3$) in 30 mL of 1,2 butanediol. The mixture was transferred to a 50 ml Teflon bottle and purged with forming gas before being sonicated in a water bath to dissolve the precursors. The bottle was then transferred to a stainless-steel hydrothermal reactor, heated at 8 °C/min to 250 °C and held at this temperature for 75 min. After the reaction, the obtained black precipitates were washed and centrifuged several times with chloroform. To control the composition, the mole ratio of Co- and Ni-laurates was adjusted appropriately to obtain $Co_{1-x}Ni_x$ alloys, where x= 0, 0.1, 0.2, 0.3, 0.4 and 0.5.

The morphology of the aligned Co nanowires was recorded using Hitachi S-4800 II Field Emission Scanning Electron Microscopy (FE-SEM) and with the Hitachi H-9500 TEM operated at an accelerated voltage of 300 kV. The magnetic properties of the samples were studied using a physical property measurement system (Quantum Design Dyanacool-PPMS). The phase of the synthesized $Co_{1-x}Ni_x$ nanowires was investigated using X-ray powder diffraction from a Rigaku Ultima IV with Cu Kα source. In order to characterize the morphology and measure the magnetic properties of $Co_{1-x}Ni_x$ nanowires, the as-prepared samples were dispersed in chloroform and then were dried on copper foil under a magnetic field of 2 Tesla. The morphology of the aligned $Co_{1-x}Ni_x$ nanowire assemblies was recorded using Hitachi S-4800 II Field Emission Scanning Electron

Microscopy (FE-SEM). The magnetic properties were measured using a Quantum Design Physical Property Measurement System (DynaCool PPMS ± 9 Tesla).

4.3 Assembly and Magnetic Properties of Co Nanowires

4.3.1 Morphology and Structural Characterization of Co Nanowires

Figure 4.1 shows the TEM images of the as-prepared Co nanowires which reveals the change in morphology of the nanowires with increasing HDA and constant $RuCl_3$ of 6 mg. When 0.2 g of HDA is used, nanowires of length 165 nm and diameter of 20 nm are obtained. When the HDA is increased, the length and diameter of the nanowires gradually decreases to a minimum of 120 nm and 10 nm, respectively, for an HDA concentration of 0.8 g. Additionally, as the HDA is increased the number of multipoles and polyhedral particles is reduced and the nanowires become more uniform. It is believed that the HDA acts as a surfactant in the Co nanowire synthesis and has preferential binding to the lateral facets of the particles.[101] The surfactant will reduce the rate of metal ions from reaching the surfaces they are bound to, preventing those surfaces from growing due to the slowed diffusion of metal ions. Since the HDA molecules prefer the lateral facets, the particles will have more preferential growth along the c-axis, (0001) direction, and promote the formation of nanowires. By increasing the HDA concentration, more HDA molecules are available

to bind onto the surface of the particles to prevent growth on the lateral facets, which helps simultaneously increase the uniformity and decrease the diameter.

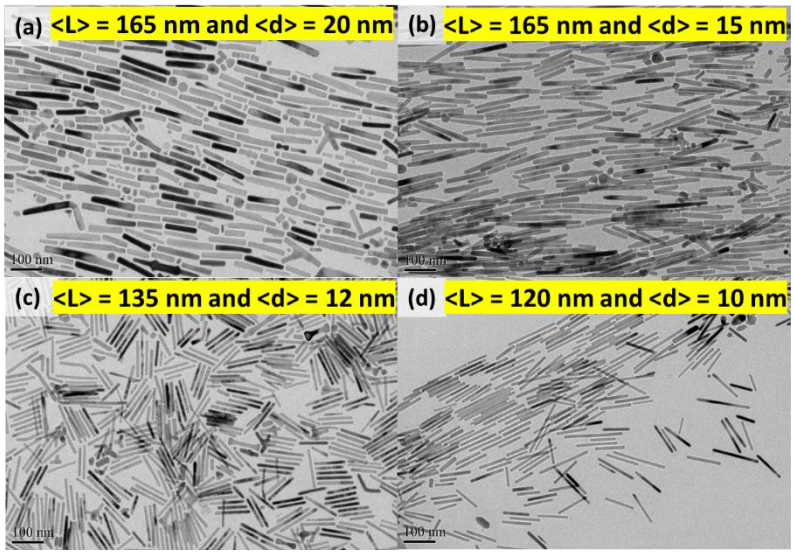

Figure 4.1 Shows the TEM images of the prepared samples using (a) 0.2 g HDA (b) 0.4 g HDA (c) 0.6 g HDA and (d) 0.8 g HDA.

Although the HDA concentrations show a decreasing trend in the nanoparticle diameter with increasing HDA up to 0.8 g, it does not follow the same trend when the HDA is increased further. It can be seen from Figure 4.2 that when the HDA is increased above 0.8 g, the nanowires become less uniform and form enlarged tips. For the HDA concentrations above 0.8 g, it is possible that the excess HDA begins to slow the growth rate of the particles. Additionally, towards the end of the reaction the growth rate is slowed due to the small amount of metal ions left in solution. The slowed growth will help favor growth on the lateral facets and lead to the enlarged tips. [102]

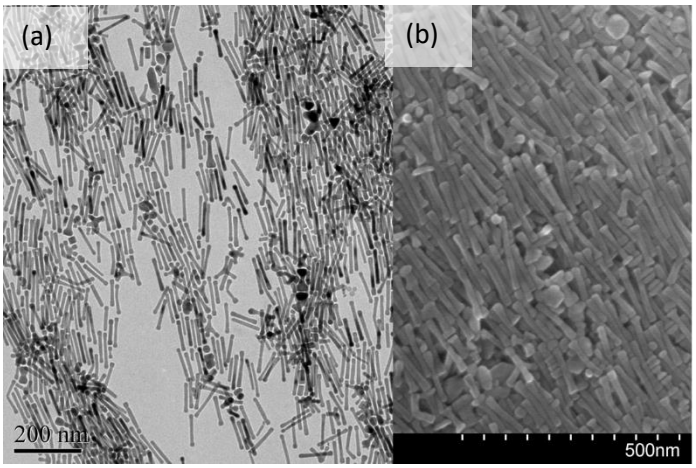

Figure 4.2 (a) shows the TEM image and (b) shows the SEM image of the Co nanowires prepared with 1 g HDA.

4.3.2 Assembly Formation and Characterization

To create aligned assemblies of the prepared nanowires, a field-assisted assembly method similar to the one used in section 3.2.2. For 2D assemblies, a high concentration of dispersed Co nanowires in chloroform are drop casted onto copper foil and allowed to dry under a constant magnetic field of 1.0 T using an electromagnet. For the 3D assemblies, the Co nanowire dispersion were transferred into an aluminum tray for a larger volume and dried under the same external field. Figure 4.3 shows the SEM images of the 20 nm, 15 nm, 12 nm, and 10 nm samples. From these images, it is seen that the nanowires are capable of forming 2D arrays with good alignment to the applied field direction. It is also obvious that the number of multipods and nanoparticles present can have a considerable negative impact on the sample alignment, demonstrating the need for

uniform morphology when creating well-ordered nanoparticle assemblies. In this case, the 10 nm nanowires exhibit the most uniform morphology and as such have the best aligned assembly.

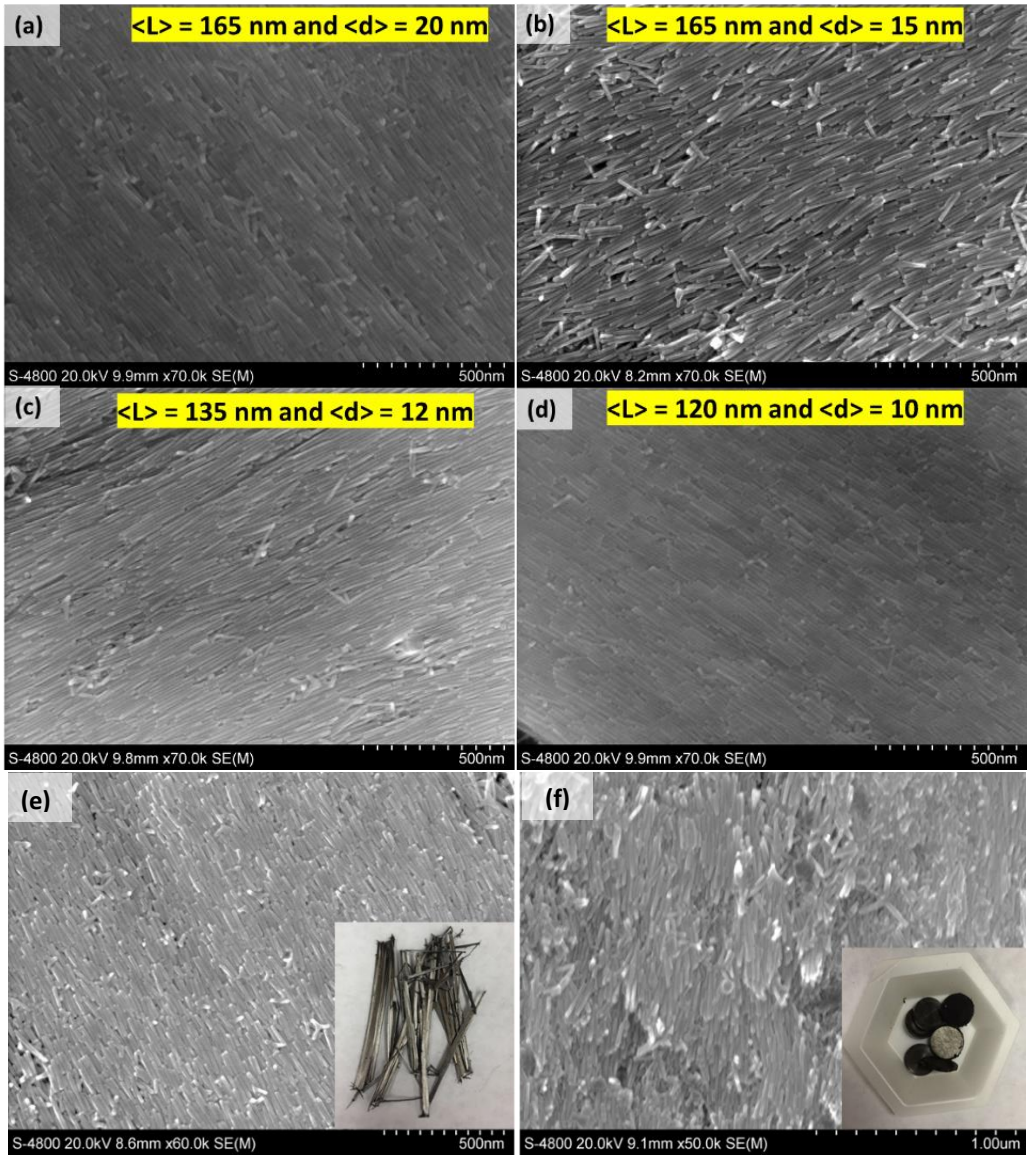

Figure 4.3 (a)-(d) The SEM images show the uniformity of the field-assisted aligned 2D assemblies for each sample. (e) and (f) show the SEM images and the bulk aligned 3D assemblies (inserts) before and after being packed.

In order to investigate the ability of these Co assemblies to make bulk 3D assemblies for permanent magnets, a large amount of Co nanowires was synthesized using the large-scale thermal decomposition method and assembled using the field-assisted assembly technique. The assemblies were then taken and compacted to create bulk dense assemblies. Before compaction, the Co nanowires assemble into elongated superstructures with long range ordering and alignment, as indicated by Figure 4.3e. After compaction, bulk pellets of the Co nanowire assemblies are obtained, however, during the compaction process the alignment is slightly reduced, as shown in Figure 4.3f.

4.3.3 Magnetic Hysteresis Characterization

To investigate the properties of the aligned assemblies, hysteresis loops were measured parallel and perpendicular to each sample, as shown by Figure 4.4. Each sample has an M_S of 150 emu/g, however, the coercivity of the assemblies is shown to have a considerable dependence on the diameter of the nanowires. As the diameter decreases from 20 nm to 10 nm, the coercivity increases from 6.3 kOe to 10.4 kOe, respectively, which is considerably higher than the theoretical magnetocrystalline anisotropy field of bulk Co materials (7.3 kOe). The improvement of the coercivity in the nanowire assemblies is primarily a result of the increased shape anisotropy developed by controlling the morphology of the nanowires. It is also important to notice that the loops become more square-like as the diameter decreases, which can lead to a significant improvement in the $(BH)_{max}$ of the assembly. As was previously shown in Figure 4.1, the increasing HDA also reduces the number of non-uniform nanoparticles, which leads to the more square-like hysteresis loops.

To demonstrate the importance of diameter and alignment in the coercivity of the assemblies, Figure 4.4e compares the coercivity of the randomly oriented and aligned assemblies

with respect to the nanowire diameter. While the coercivity increases with decreasing diameter for both the random and aligned assemblies, the coercivity is considerably lower for the random assemblies in every case.

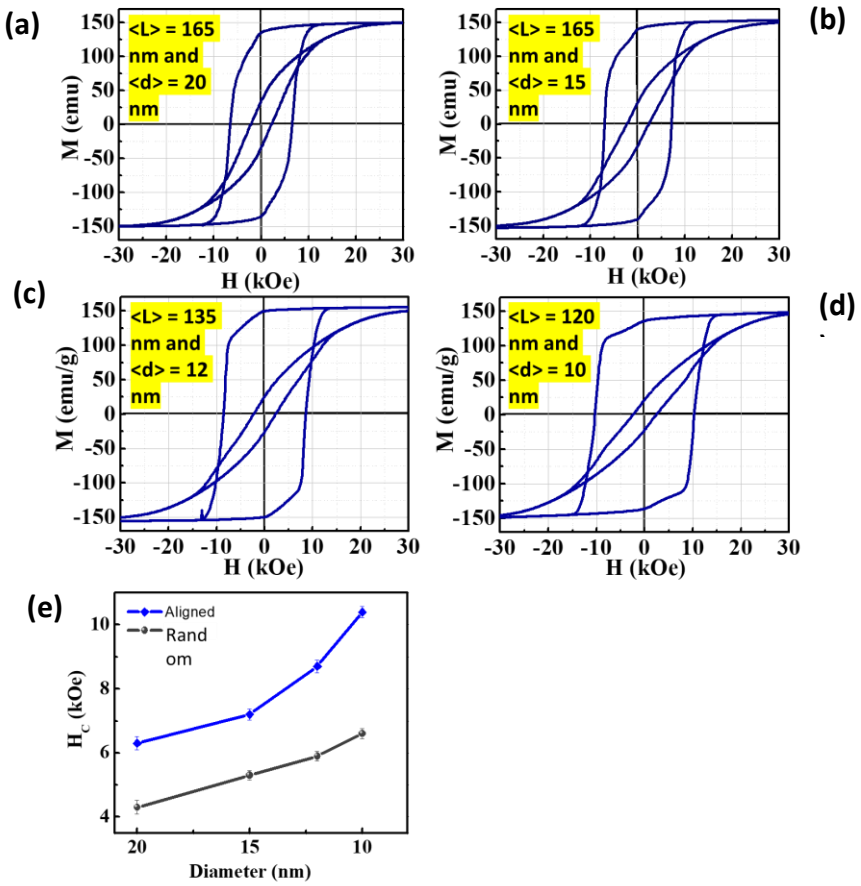

Figure 4.4 (a-f) Show the hysteresis loops measured for each sample parallel and perpendicular to the aligned direction. (e) Compares the coercivity vs diameter for the random assemblies and aligned assemblies at room temperature.

4.3.4 Co/FeCo Nanocomposite

In order to effectively exchange couple a soft-magnetic material to a hard-magnetic material, one of the more important factors to consider is the size of the soft-magnetic material. In general, the thickness of the soft-magnetic material needs to be smaller than twice the domain wall size of the hard-magnetic material.[11,103,104] Exchange-coupled nanocomposites are commonly core-shell type structures with controlled core size and shell thickness.[105-107] However, many of the methods used to synthesize these core-shell composites use high temperatures to create the coatings. In the case of Co nanowires, the hcp crystal structure and nanowire morphology are not stable for high temperature reactions, which limits the available methods for coating. Therefore, we use the electroless method that uses a strong reducing agent to reduce the metal precursors to prevent the need for high temperatures. After optimizing the HDA concentration for the Co nanowires synthesis, the 0.8 g HDA sample was used for coating with FeCo. The TEM images of the as-prepared nanowires (Figure 4.5a) and the nanowires after coating (Figure 4.5b) are shown. It is clearly seen that the FeCo was able to coat the surface of bundled Co nanowires without losing their shape anisotropy. The magnetic properties were then measured for two samples of different FeCo coating thickness, shown in Figure 4.5c. The M_S of the pure Co nanowires is 150 emu/g, however, when the volume fraction of the coating is increased (f), the magnetization increases to 170 emu/g for f = 0.2 and 182 emu/g for f = 0.3. The absence of large kinks in the curves also indicate that the FeCo is effectively exchange coupled to the Co nanowires.

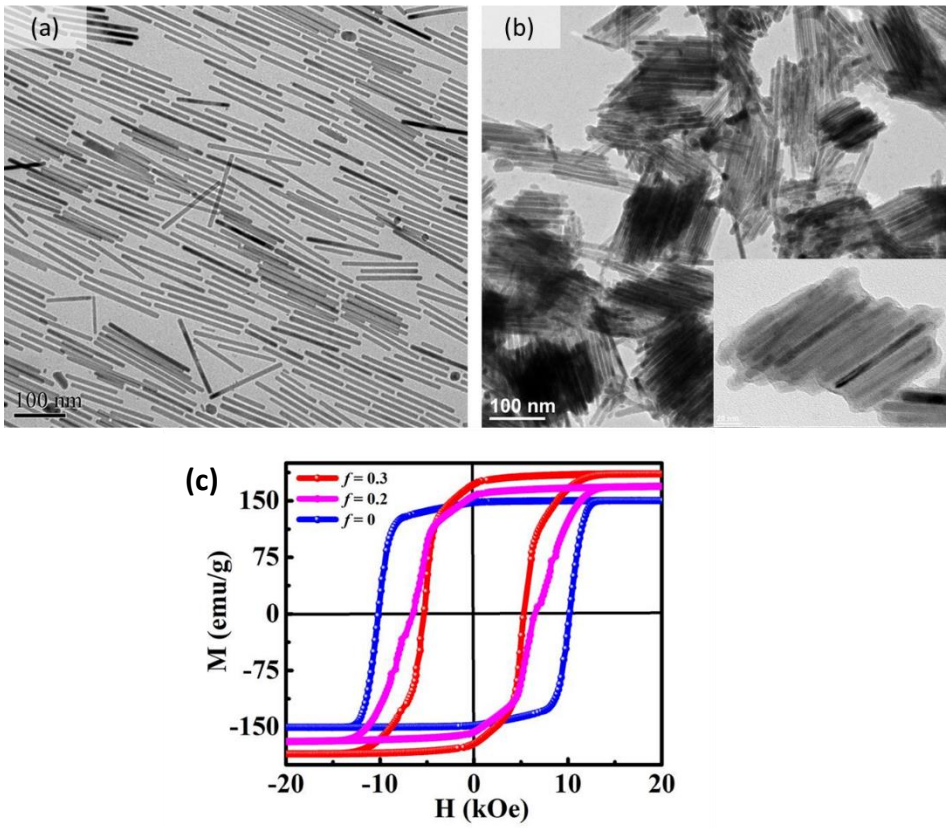

Figure 4.5 The TEM images of the nanowires (a) before coating and (b) after coating with FeCo with the inset showing the high-magnification TEM image. (c) The hysteresis loops of the Co nanowires with different FeCo coating volume fractions (*f*), which shows the enhancement of magnetization with increasing FeCo.

4.4 Magnetic Hardening in CoNi Nanowire Assemblies

4.4.1 Morphology and Structural Characterization

Figure 4.6 shows the XRD patterns for the as-synthesized $Co_{1-x}Ni_x$ nanowires/nanoparticles. When $x \leq 0.3$, all the peaks match well with the standard XRD patterns of hcp-CoNi phase. The increase of Ni content above x = 0.3 leads to the formation of both fcc and hcp CoNi phases, which can be seen from the XRD patterns of the $Co_{0.6}Ni_{0.4}$ sample. When

the Ni content is increased to x = 0.5, the diffraction peaks corresponding to the hcp structure completely disappear, which shows the formation of a pure fcc structure $Co_{0.5}Ni_{0.5}$ alloy. The phase evolution in nanowires/nanoparticles via modulation of Ni content is congruent with the standard phase diagram of CoNi alloys, according to which the presence of fcc CoNi is expected above the Ni compositions x =0.3.

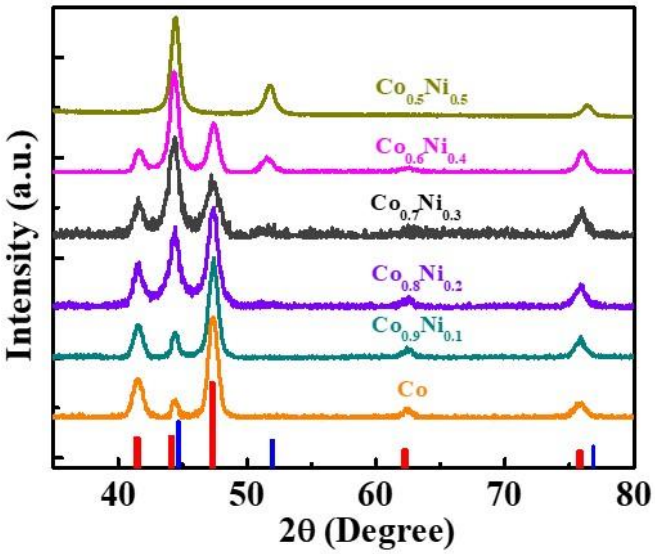

Figure 4.6 XRD patterns for Co1-xNix alloys (x= 0, 0.1, 0.2, 0.3, 0.4 and 0.5). Red and blue bars represent the standard XRD patterns of hcp and fcc structured CoNi alloys, respectively.

Figure 4.7 shows the SEM micrographs of the aligned $Co_{1-x}Ni_x$ nanowire/nanoparticle assemblies. It clearly confirms that the synthesized sample morphology is strongly affected by the modulation of Ni content. For instance, the wire shape morphology is retained up to Ni content of x = 0.3, the increase of Ni content to x =0.4 leads to the formation of nanoparticles, and a further increase of Ni content to x = 0.5 results in formation of spherical shaped nanoparticle aggregates. As we know, the intrinsically anisotropic hcp structure favors growth along the c-axis, i.e easy

magnetization axis of hcp-Co or CoNi. In our synthesis process, the long-chain amine molecules adsorb more favorably on the lateral facets, which supports growth along the inefficiently passivated {0001} basal facet.[101] The preferred c-axis growth facilitates formation of perfect single crystals with wire-shaped morphology. On the other hand, the fcc structure prefers to grow along the {111} and {100} facets, which results in the formation of polyhedron shaped nanoparticles like cubes, octahedrons or quasi-spherical morphologies. So, when Ni content increases above x = 0.4, the particle morphology alters to nanorods with dumbbell like tips and polyhedron shapes as shown in Figure 4.7f. In addition to the shape modulation, the uniformity and the aspect ratio of $Co_{1-x}Ni_x$ nanowires are also affected by the variation of Ni content from x = 0 to x = 0.3. For example, the average diameter of the nanowires is increased from 10 nm to 12 nm and the length is decreased from 160 nm to 75 nm with increase of Ni content.

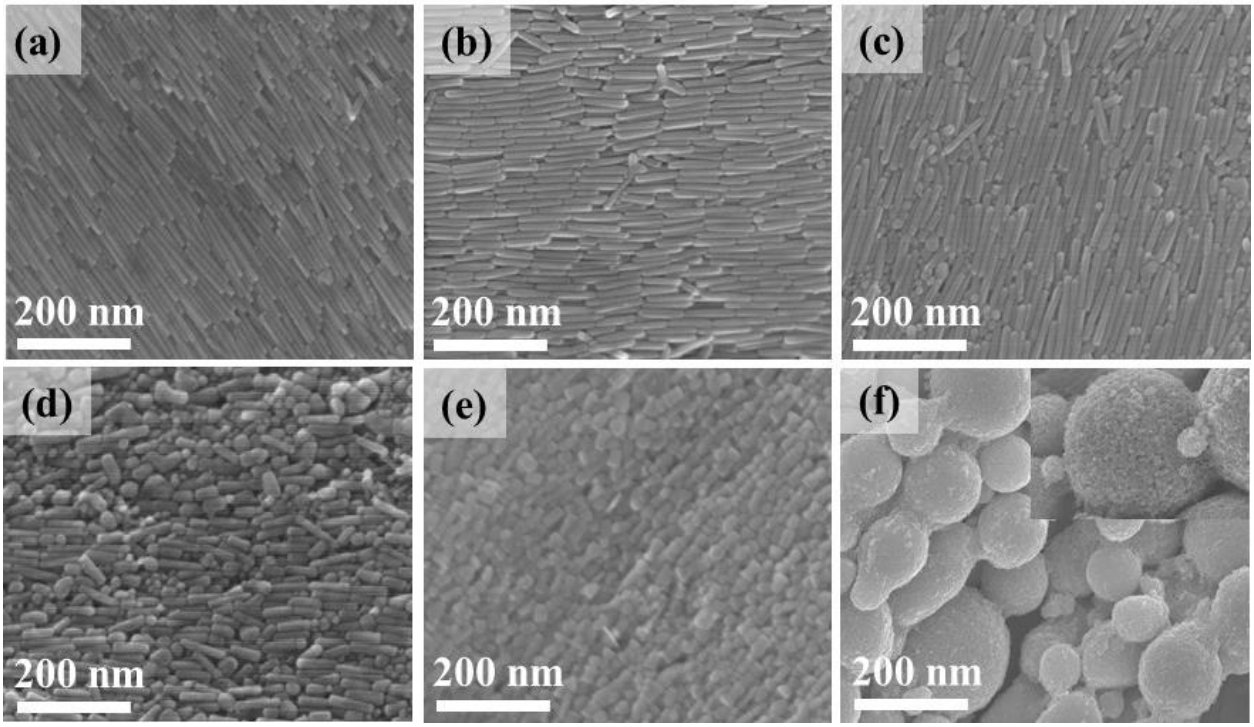

Figure 4.7 SEM micrographs of aligned nanowire (or nanoparticle) assemblies for (a) Co, (b) $Co_{0.9}Ni_{0.1}$, (c) $Co_{0.8}Ni_{0.2}$, (d) $Co_{0.7}Ni_{0.3}$, (e) $Co_{0.6}Ni_{0.4}$, and (f) $Co_{0.5}Ni_{0.5}$, respectively. Inset of the figure (f) shows the high-resolution SEM micrograph of $Co_{0.5}Ni_{0.5}$ nanoparticles.

To further investigate the change in morphology with increasing Ni content, two samples were prepared for HRTEM by drop casting a dispersed solution of pure Co and $Co_{0.7}Ni_{0.3}$ onto separate copper grids. As shown in Figure 4.8, there is a clear difference in the crystallinity and morphology of the two samples. The pure Co sample, Figure 4.8a-c, displays a smooth surface, pristine crystal structure, and round tips. In contrast, the $Co_{0.7}Ni_{0.3}$ sample, Figure 4.8d-f, has a rough surface, stacking faults, and enlarged faceted tips that contain fcc crystal structures. The imperfections seen in the $Co_{0.7}Ni_{0.3}$ sample are primarily a result of the Ni addition. Because Ni prefers to grow in the fcc phase, the addition of Ni into the Co nanowires promotes the formation of fcc stacking in the hcp lattice. Additionally, it has been previously reported that there is an

increase in lateral growth around the sites of stacking faults due to the displacement of surface capping long chain molecules, which in turn allow Co and Ni ions to diffuse more readily into the lateral facets.[108] This leads to both the increased diameter seen in Figure 4.7 and the rough surface seen in Figure 4.8d and 4.8e. As for the enlarged tips, it is well understood that towards the end of the reaction there are fewer available ions in solution, which in turn leads to a slower growth rate.[102] The diameter of hcp Co is affected by the growth rate; typically, slower growth rates lead to larger diameters. For samples with higher Ni content, the slower growth rate at the end of the reaction combined with the stacking faults induced by Ni helps facilitate growth perpendicular to the c-axis, leading to the enlarged tips. The presence of stacking faults in the $Co_{0.7}Ni_{0.3}$ is further confirmed by the FFT pattern in Figure 4.8f. The presence of multiple bright spots around the zones corresponding to the different crystallographic planes indicate the presence of atomic layers that are slightly displaced from the typical positions.[109] The displaced layers can be correlated to the stacking faults induced by the Ni.

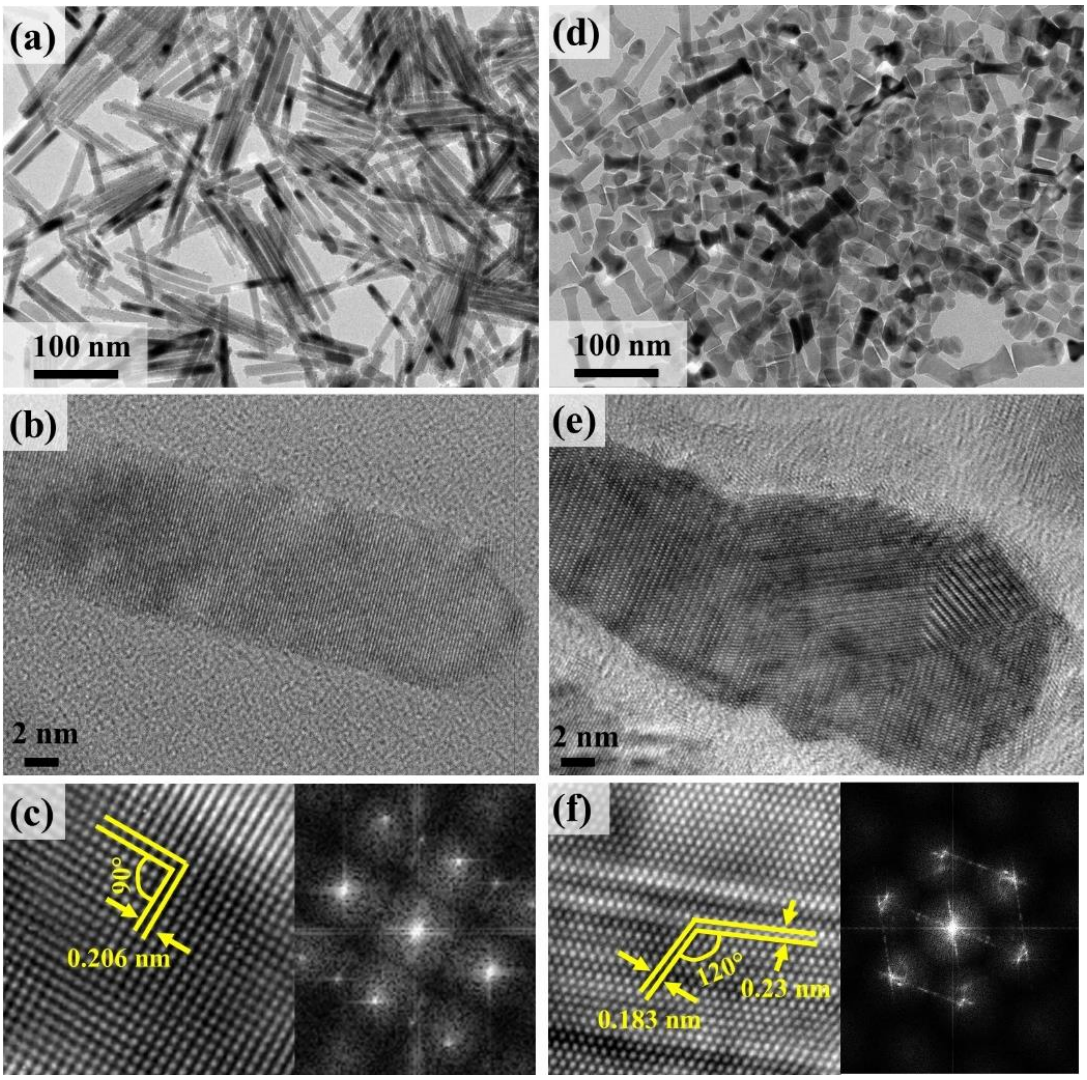

Figure 4.8 TEM analysis of cobalt nanowires. (a) Bright-field TEM image of pristine Co nanowires, (b) high resolution TEM image of a single nanowire and (c) the corresponding numerical FFT and IFFT pattern. (d) Bright-field TEM image of $Co_{0.7}Ni_{0.3}$ nanowires, (b) high resolution TEM image of a single nanowire and (c) the corresponding numerical FFT and IFFT pattern.

4.4.2 Magnetic Hysteresis and $(BH)_{max}$ Characterization

The magnetic properties of the aligned $Co_{1-x}Ni_x$ nanowire/nanoparticles assemblies are shown in Figure 4.9, systematically showing the dependence of M_S, H_C and $(BH)_{max}$ with the variation of Ni content. The obvious shape anisotropy behaviors are observed, which enhances the coercivity to 11.4 kOe for pristine Co nanowires and the coercivity value decreases monotonously with increase of the Ni content (see Figure 4.9a). In a similar way, the saturation magnetization (M_S, 148 emu/g to 96 emu/g) and the remanence magnetization (M_R, 142 emu/g to 80 emu/g) decrease with increase of Ni content from x =0 to x = 0.5. The decreasing trend in coercivity is related to the effective magnetic anisotropy, which decreases with increase of Ni content as a combined result of the declining magnetocrystalline anisotropy, loss of nanowire morphology, and increase of stacking faults. The decrease in magnetization values are attributed to the lower magnetic moment of Ni (0.6 μ_B) compared to Co (1.72 μ_B).[110] Here, it should be mentioned that the M_R/Ms ratio decreases with the Ni addition, which indicates that there exist some low coercivity materials together with the high coercivity nanowires/nanorods. The SEM images indicate that the low coercivity materials are the nanoparticles that form when the Ni content is increased. More importantly, the coercivity of the $Co_{0.6}Ni_{0.4}$ (4.4 kOe) and $Co_{0.5}Ni_{0.5}$ (1.9 kOe) alloys are higher than that expected for fcc structured alloys. The high coercivity in these fcc structured alloys may be related to the presence of some nanoparticles with anisotropic morphology. In short, the shape anisotropy in the entire concentration range of Ni has played a substantial role in developing coercivity. Thus, the synthesized $Co_{1-x}Ni_x$ alloys can be used as building blocks for nanostructured rare-earth-free permanent magnet.

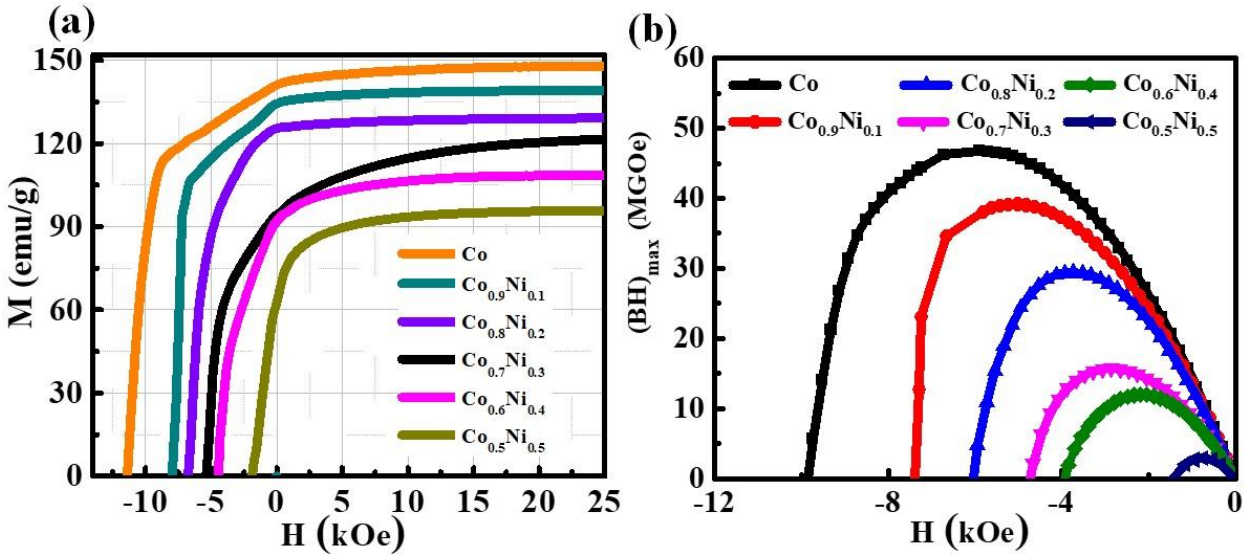

Figure 4.9 (a) M-H plots of the second quadrant and b) $(BH)_{max}$ curves of the aligned $Co_{1-x}Ni_x$ nanoparticle assemblies.

In order to show the efficacy of the $Co_{1-x}Ni_x$ nanowires for permanent magnet applications, the energy product of the aligned nanowires assemblies is estimated based on a 100 percent volume fraction of closely packed Co nanowires using their theoretical density, as shown in Figure 4.9b. The $(BH)_{max}$ of the aligned assemblies is reduced from 47 to 2.9 MGOe with increase of Ni content from x = 0 to 0.5, respectively. Especially, when the Ni content is increased beyond x =0.2, the $(BH)_{max}$ values are reduced drastically, however, it should be noted that the $(BH)_{max}$ values are record high for critical rare-earth- or expensive Pt-free hard magnetic materials. This trend is in congruence with the H_C and M_R/Ms ratio variation with the Ni content. Importantly, since the nanoparticle content increased with addition of Ni, the M_R/Ms ratio decreased and consequently resulted in low energy products. Our experimental findings open up an avenue for developing coercivity in soft-magnetic alloys and also show a potential direction to the development of next generation permanent magnets.

4.5 Conclusion

A thermal decomposition approach was used produce Co nanowires with uniform morphology. Using this method, the nanowires can be produced on a larger scale, allowing for more rapid production that would be favorable for commercial use. Additionally, the simplicity of the reaction allowed for easy modulation of the HDA to efficiently determine the optimal concentration for small diameter nanowires. By controlling the HDA concentration, the diameters of the nanowires could be reduced to as low as 10 nm and the coercivity of the nanowires was shown to increase with the decrease of the nanowire diameter, up to 10.4 kOe for the 10 nm nanowires. The 10 nm nanowires were then successfully coated with FeCo using an electroless coating method. The morphology of the nanowires was retained during the reaction and the magnetization was increased from 150 emu/g to 182 emu/g. Therefore, coating the Co nanowires with FeCo is a promising route to preparing rare-earth-free magnetic materials.

$Co_{1-x}Ni_x$ nanowires and nanoparticles with controlled Ni concentration were synthesized via a solvothermal approach. For Ni concentration below x = 0.3, the preferential growth along the c-axis of hcp structure forms hcp $Co_{1-x}Ni_x$ nanowires with enhanced effective magnetic anisotropy. The synergy of the magnetocrystalline anisotropy and the shape anisotropy give rise to the prominent coercivity (11.4 to 5.4 kOe) and thus high energy product (47.8 to 18.1 MGOe) of $Co_{1-x}Ni_x$ nanowires (x= 0 to 0.3). However, when x > 0.3, the hcp phase, shape anisotropy, and consequently the magnetic properties are reduced noticeably due to the increased fcc CoNi. At x = 0.5, the shape changes to spherical particles, the particles become purely fcc, and the magnetic hardening is considerably low. The $Co_{1-x}Ni_x$ nanowires with x = 0.3 are particularly interesting, as the nanowires retain their shape anisotropy and magnetic properties. These nanowires

demonstrate the ability to develop high coercivity in rare-earth-free magnetic materials that can be used in the production of intermediate permanent magnets.

CHAPTER 5 Summary and Future Scopes

5.1 Summary

The intrinsic and extrinsic magnetic properties of Co make it an attractive and important element in magnetic materials. It has remained a staple element in many magnetic materials throughout the history of magnetic material development and continues to play a significant role in new and emerging nanostructured materials. Recently, it has been of particular interest in the development of magnetically hard nanostructured materials. In particular, the ability to develop coercivity by exploiting the shape anisotropy has shown potential in the design of rare-earth-free permanent magnets. Additionally, Co containing compounds demonstrate unique interparticle interactions on the nanoscale, which has gained the interest of investigations of assemblies and superstructures built from nanoparticles. The work presented focuses on the development and investigation of magnetic Co containing nanostructured materials including Co alloys, composites, and ferrites. The magnetic properties were tuned and even enhanced by controlling the morphology and assembly process, and by exchange coupling with FeCo. To briefly summarize:

- The surface effects and magnetic properties of $CoFe_2O_4$ nanoparticles of sizes 3.5 and 16 nm in their respective assemblies are investigated. It is demonstrated that the 3.5 nanoparticles exhibit increased coercivity at low temperatures, which is confirmed to be a result of super spin-glass behavior.
- The intrinsic properties of $CoFe_2O_4$ nanoparticles has been improved by synthesizing FeCo/$CoFe_2O_4$ core-shell nanocomposite nanoparticles. The individual nanoparticles have increased magnetization of up to 108 emu/g and, consequently, increased interparticle interactions when assembled. Additionally, the investigation of the assembly process and

superstructures revealed an increase in coercivity for the field-assisted assemblies at low temperature (5 K).

- Co nanowires with various diameters have been synthesized with a modified thermal decomposition approach. The individual nanoparticles demonstrated high H_C due to the high shape anisotropy. Long range ordered assemblies are obtained and demonstrated to be capable of being compacted into bulk samples with reasonable magnetic properties. Additionally, the improvement of the magnetization of the Co nanowires has been investigated by coating the nanowires with FeCo, which achieved a saturation magnetization as high as 182 emu/g.
- Finally, the improvement of coercivity in $Co_{1-x}Ni_x$ alloys has been investigated by synthesizing $Co_{1-x}Ni_x$ nanowires with high shape anisotropy. The variation in the crystal structure, morphology, and magnetic properties of CoNi nanoparticles are systematically studied for assemblies of CoNi nanoparticles with varying Ni concentration. The dependence of the magnetic performance on the Ni concentration for each sample was then investigated by determining and comparing the $(BH)_{max}$, which showed that reasonable $(BH)_{max}$ values can be retained for Ni concentrations up to $x = 0.3$.

5.2 Future Scopes

The work presented in this thesis has demonstrated that there are still ways to develop new nanostructured magnetic materials with enhanced magnetic properties. There are several combinations of materials that can be exchange-coupled, synthesized with shape anisotropy, or synthesized with a combination of the two that have potential. For example, $CoFe_2O_4$ can achieve higher coercivity values if the nanoparticles are synthesized with high shape anisotropy. Combining the high shape anisotropy with the exchange-coupled composite would create a

nanostructured material with not only enhanced coercivity, but also high magnetization, which would lead to a greatly enhanced energy product. Additionally, other ferrites such as barium ferrite are also capable of reaching high coercivity values, so that exchange coupling with FeCo would also be a potential route to the development of a high energy product. The control over shape anisotropy also has high potential in other magnetic materials such as Fe or FeCo, which already has a high intrinsic magnetization and would greatly benefit from increased coercivity. Needless to say, the development of new nanostructured magnetic materials is still an ongoing effort with several approaches and opportunities to achieve better magnetic performance.

References

1. Mohn, Peter. *Magnetism in the solid state: an introduction*. Vol. 134. Springer Science & Business Media, 2006.
2. Griffiths, David J. *Introduction to Electrodynamics*. 4th ed., Cambridge University Press, 2017.
3. Cullity, Bernard Dennis, and Chad D. Graham. *Introduction to magnetic materials*. John Wiley & Sons, 2011.
4. Tilley, Richard JD, and R. J. D. Tilley. *Understanding solids: the science of materials*. Hoboken: Wiley, 2013.
5. Ling, Samual J., et al. "University Physics Volume 2." (2016).
6. Sinatra, Francy L. "Understanding the interaction between blood flow and an applied magnetic field." (2010).
7. Hook, J. R., and H. E. Hall. "Solid state physics" 2nd Edition. (2001).
8. Landau, Lev Davidovich, et al. *Electrodynamics of continuous media*. Vol. 8. elsevier, 2013.
9. Hall, R. C. "Single crystal anisotropy and magnetostriction constants of several ferromagnetic materials including alloys of NiFe, SiFe, AlFe, CoNi, and CoFe." *Journal of Applied Physics* 30.6 (1959): 816-819.
10. Kittel, Charles. "Physical theory of ferromagnetic domains." *Reviews of modern Physics* 21.4 (1949): 541.
11. Skomski, Ralph, and J. M. D. Coey. "Giant energy product in nanostructured two-phase magnets." *Physical Review B* 48.21 (1993): 15812.

12. Walker, Michael M., et al. "Structure and function of the vertebrate magnetic sense." *Nature* 390.6658 (1997): 371-376.
13. Krahne, Roman, et al. "Physical properties of elongated inorganic nanoparticles." *Physics Reports* 501.3-5 (2011): 75-221.
14. Vestal, Christy R., and Z. John Zhang. "Effects of surface coordination chemistry on the magnetic properties of $MnFe_2O_4$ spinel ferrite nanoparticles." *Journal of the American Chemical Society* 125.32 (2003): 9828-9833.
15. Stoner, Edmund C. "XCVII. The demagnetizing factors for ellipsoids." *The London, Edinburgh, and Dublin philosophical magazine and journal of science* 36.263 (1945): 803-821.
16. Osborn, J. A. "Demagnetizing factors of the general ellipsoid." *Physical review* 67.11-12 (1945): 351.
17. Stoner, E. C., and E. P. Wohlfarth. "Interpretation of high coercivity in ferromagnetic materials." *Nature* 160.4071 (1947): 650-651.
18. Kuncser, A., and V. Kuncser. "Magnetization reversal via a Stoner–Wohlfarth model with bi-dimensional angular distribution of easy axis." *Journal of Magnetism and Magnetic Materials* 395 (2015): 34-40.
19. Mohapatra, Jeotikanta, et al. "Superspin glass behavior of self-interacting CoFe2O4 nanoparticles." *Journal of Alloys and Compounds* 628 (2015): 416-423.
20. Mishima, T. "Nickel-aluminum steel for permanent magnets." *Ohm* 19 (1932): 353.
21. Strnat, K., et al. "A family of new cobalt-base permanent magnet materials." *Journal of Applied Physics* 38.3 (1967): 1001-1002.

22. Tang, Hao, Mohammad Aref Hasen Mamakhel, and Mogens Christensen. "Enhancing the coercivity of SmCo 5 magnet through particle size control." *Journal of Materials Chemistry C* 8.6 (2020): 2109-2116.
23. Coey, J. M. D. "Permanent magnetism." *Solid State Communications* 102.2-3 (1997): 101-105.
24. Gutfleisch, Oliver. "Controlling the properties of high energy density permanent magnetic materials by different processing routes." *Journal of Physics D: Applied Physics* 33.17 (2000): R157
25. Tancredi, Pablo, et al. "Significant coercivity enhancement at low temperatures in magnetically oriented cobalt ferrite nanoparticles." *Applied Physics Letters* 115.26 (2019): 263104.
26. Kubisztal, M., et al. "Collective Superspin Glass State of Interacting Cobalt Ferrite Nanoparticles." *IEEE Transactions on Magnetics* 55.12 (2019): 1-6.
27. Gandha, Kinjal, et al. "High energy product developed from cobalt nanowires." *Scientific reports* 4.1 (2014): 1-5.
28. Bunker, B. C., et al. "Ceramic thin-film formation on functionalized interfaces through biomimetic processing." *Science* 264.5155 (1994): 48-55.
29. Lifshitz, Ilya M., and Vitaly V. Slyozov. "The kinetics of precipitation from supersaturated solid solutions." *Journal of physics and chemistry of solids* 19.1-2 (1961): 35-50.
30. Vreeland, Erika C., et al. "Enhanced nanoparticle size control by extending LaMer's mechanism." *Chemistry of Materials* 27.17 (2015): 6059-6066.

31. Murray, C Bea, David J. Norris, and Moungi G. Bawendi. "Synthesis and characterization of nearly monodisperse CdE (E= sulfur, selenium, tellurium) semiconductor nanocrystallites." *Journal of the American Chemical Society* 115.19 (1993): 8706-8715.
32. Sugimoto, Tadao. "Preparation of monodispersed colloidal particles." *Advances in Colloid and Interface Science* 28 (1987): 65-108.
33. Sun, Shouheng, et al. "Monodisperse MFe_2O_4 (M= Fe, Co, Mn) nanoparticles." *Journal of the American Chemical Society* 126.1 (2004): 273-279.
34. Mitra, Arijit, et al. "Verwey transition in ultrasmall-sized octahedral Fe3O4 nanoparticles." *The Journal of Physical Chemistry C* 118.33 (2014): 19356-19362.
35. Porter, David A., and Kenneth E. Easterling. *Phase transformations in metals and alloys (revised reprint)*. CRC press, 2009.
36. Cordente, Nadege, et al. "Synthesis and magnetic properties of nickel nanorods." *Nano letters* 1.10 (2001): 565-568.
37. Khurshid, Hafsa, et al. "Mechanism and controlled growth of shape and size variant core/shell FeO/Fe 3 O 4 nanoparticles." *Nanoscale* 5.17 (2013): 7942-7952.
38. Puntes, Victor F., et al. "Synthesis of hcp-Co nanodisks." *Journal of the American Chemical Society* 124.43 (2002): 12874-12880.
39. Deatsch, Alison E., and Benjamin A. Evans. "Heating efficiency in magnetic nanoparticle hyperthermia." *Journal of Magnetism and Magnetic Materials* 354 (2014): 163-172.
40. Bao, Ningzhong, et al. "Formation mechanism and shape control of monodisperse magnetic $CoFe_2O_4$ nanocrystals." *Chemistry of Materials* 21.14 (2009): 3458-3468.

41. Chen, Yuanzhi, et al. "Preparation and magnetic properties of nickel nanoparticles via the thermal decomposition of nickel organometallic precursor in alkylamines." *Nanotechnology* 18.50 (2007): 505703.
42. Murray, Christopher B., et al. "Colloidal synthesis of nanocrystals and nanocrystal superlattices." *IBM Journal of Research and Development* 45.1 (2001): 47-56.
43. Rabenau, Albrecht. "The role of hydrothermal synthesis in preparative chemistry." *Angewandte Chemie International Edition in English* 24.12 (1985): 1026-1040.
44. Fievet, F., J. P. Lagier, and M. Figlarz. "Preparing monodisperse metal powders in micrometer and submicrometer sizes by the polyol process." *Mrs Bulletin* 14.12 (1989): 29-34.
45. Fiévet, F., et al. "The polyol process: a unique method for easy access to metal nanoparticles with tailored sizes, shapes and compositions." *Chemical Society Reviews* 47.14 (2018): 5187-5233.
46. Ung, D., et al. "Growth of magnetic nanowires and nanodumbbells in liquid polyol." *Chemistry of materials* 19.8 (2007): 2084-2094.
47. Harris, V. G., et al. "High coercivity cobalt carbide nanoparticles processed via polyol reaction: a new permanent magnet material." *Journal of Physics D: Applied Physics* 43.16 (2010): 165003.
48. Feldmann, Claus, and Hans-Otto Jungk. "Polyol-mediated preparation of nanoscale oxide particles." *Angewandte Chemie International Edition* 40.2 (2001): 359-362.
49. Hou, Y., et al. "Size-controlled synthesis of nickel nanoparticles." *Applied Surface Science* 241.1-2 (2005): 218-222.

50. Zoriasatain, S et al. Magnetic Anisotropies in FeCo Fine Particles. *Journal of magnetism and magnetic materials.* 300.2 (2006): 525–531.
51. Sun, Yuan-Pang, et al. "Characterization of zero-valent iron nanoparticles." *Advances in colloid and interface science* 120.1-3 (2006): 47-56.
52. Carroll, Kyler J., et al. "Annealing of amorphous Fe_xCo_{100-x} nanoparticles synthesized by a modified aqueous reduction using $NaBH_4$." *Journal of Applied Physics* 107.9 (2010): 09A303.
53. Cullity, Bernard Dennis. *Elements of X-ray Diffraction*. Addison-Wesley Publishing, 1956.
54. Lenormand, Denny R. "Characterization of Magnetic Nanostructured Materials by First Order Reversal Curve Method." (2012).
55. Zhang, Lei, Hao Bin Wu, and Xiong Wen Lou. "Iron-oxide-based advanced anode materials for lithium-ion batteries." *Advanced Energy Materials* 4.4 (2014): 1300958.
56. Mohapatra, Jeotikanta, Meiying Xing, and J. Ping Liu. "Inductive thermal effect of ferrite magnetic nanoparticles." *Materials* 12.19 (2019): 3208.
57. Mathieu, Roland, et al. "Phase transition in a super superspin glass." *EPL (Europhysics Letters)* 102.6 (2013): 67002.
58. Kodama, Richard H., et al. "Surface spin disorder in $NiFe_2O_2$ nanoparticles." *Physical Review Letters* 77.2 (1996): 394.
59. Alves, C. R., et al. "Superparamagnetic relaxation evidences large surface contribution for the magnetic anisotropy of $MnFe_2O_4$ nanoparticles of ferrofluids." *Journal of materials science* 42.7 (2007): 2297-2303.
60. Khurshid, Hafsa, et al. "Surface spin disorder and exchange-bias in hollow maghemite nanoparticles." *Applied Physics Letters* 101.2 (2012): 022403.

61. Parker, D., et al. "Spin-glass behavior in an interacting γ-Fe 2 O 3 nanoparticle system." *Physical Review B* 77.10 (2008): 104428.
62. Djurberg, Claes, et al. "Dynamics of an interacting particle system: evidence of critical slowing down." *Physical review letters* 79.25 (1997): 5154.
63. Suzuki, Masatsugu, et al. "Observation of superspin-glass behavior in Fe_3O_4 nanoparticles." *Physical Review B* 79.2 (2009): 024418.
64. Ulrich, Markus, et al. "Slow relaxation in ferromagnetic nanoparticles: indication of spin-glass behavior." *Physical Review B* 67.2 (2003): 024416.
65. Kleemann, W., et al. "Interacting ferromagnetic nanoparticles in discontinuous $Co_{80}Fe_{20}/Al_2O_3$ multilayers: From superspin glass to reentrant superferromagnetism." *Physical Review B* 63.13 (2001): 134423.
66. Mohapatra, Jeotikanta, et al. "Size-dependent magnetic and inductive heating properties of Fe_3O_4 nanoparticles: scaling laws across the superparamagnetic size." *Physical Chemistry Chemical Physics* 20.18 (2018): 12879-12887.
67. Martinez, B., et al. "Low temperature surface spin-glass transition in γ-Fe 2 O 3 nanoparticles." *Physical Review Letters* 80.1 (1998): 181.
68. Peddis, D., et al. "Spin-glass-like freezing and enhanced magnetization in ultra-small CoFe2O4 nanoparticles." *Nanotechnology* 21.12 (2010): 125705.
69. Morales, M. P., et al. "Surface and internal spin canting in γ-Fe2O3 nanoparticles." *Chemistry of Materials* 11.11 (1999): 3058-3064.
70. Lee, K, et al. "External magnetic field dependent shift of superparamagnetic blocking temperature due to core/surface disordered spin interactions." *Nanotechnology* 28.7 (2017): 075710.

71. Peddis, D, et al. "Beyond the effect of particle size: influence of CoFe2O4 nanoparticle arrangements on magnetic properties." *Chemistry of Materials* 25.10 (2013): 2005-2013.
72. Sasaki, M., et al. "Aging and memory effects in superparamagnets and superspin glasses." *Physical Review B* 71.10 (2005): 104405.
73. Routh, Alexander F. "Drying of thin colloidal films." *Reports on Progress in Physics* 76.4 (2013): 046603.
74. Wen, Tianlong, et al. "Manipulate the magnetic anisotropy of nanoparticle assemblies in arrays." *Journal of colloid and interface science* 497 (2017): 14-22.
75. Sabsabi, Z., et al. "Interplay between surface anisotropy and dipolar interactions in an assembly of nanomagnets." *Physical Review B* 88.10 (2013): 104424.
76. Aslibeiki, B., et al. "Superspin glass state in MnFe2O4 nanoparticles." *Journal of Magnetism and Magnetic Materials* 322.19 (2010): 2929-2934.
77. Dormann, J. L., D. Fiorani, and E. Tronc, "Magnetic relaxation in fine-particle systems." *Adv Chem Phys* 283 (1997): 283-449.
78. Dormann, J. L., D. Fiorani, and E. Tronc. "On the models for interparticle interactions in nanoparticle assemblies: comparison with experimental results." *Journal of Magnetism and Magnetic Materials* 202.1 (1999): 251-267.
79. Jonsson, Petra E. "Superparamagnetism and spin glass dynamics of interacting magnetic nanoparticle systems." *Advances in Chemical Physics* 128 (2004): 191-248.
80. Nadeem, Kashif, et al. "Effect of dipolar and exchange interactions on magnetic blocking of maghemite nanoparticles." *Journal of Magnetism and Magnetic Materials* 323.15 (2011): 1998-2004.

81. Parekh, Kinnari, and Ramesh V. Upadhyay. "Static and dynamic magnetic properties of monodispersed $Mn_{0.5}Zn_{0.5}Fe_2O_4$ nanomagnetic particles." *Journal of Applied Physics* 107.5 (2010): 053907.
82. Bittova, B., et al. "Relaxation phenomena in ensembles of CoFe2O4 nanoparticles." *Journal of magnetism and magnetic materials* 324.6 (2012): 1182-1188.
83. Singh, V., M. S. Seehra, and J. Bonevich. "ac susceptibility studies of magnetic relaxation in nanoparticles of Ni dispersed in silica." *Journal of Applied Physics* 105.7 (2009): 07B518.
84. De Toro, J. A., et al. "A nanoparticle replica of the spin-glass state." *Applied Physics Letters* 102.18 (2013): 183104.
85. Poudyal, Narayan, et al. "Self-nanoscaling in FeCo alloys prepared via severe plastic deformation." *Journal of alloys and compounds* 521 (2012): 55-59.
86. Poudyal, Narayan, Chuan-bing Rong, and J. Ping Liu. "Morphological and magnetic characterization of Fe, Co, and FeCo nanoplates and nanoparticles prepared by surfactants-assisted ball milling." *Journal of Applied Physics* 109.7 (2011): 07B526.
87. Nesbitt, E. A., and H. J. Williams. "Shape and crystal anisotropy of Alnico 5." *Journal of Applied Physics* 26.10 (1955): 1217-1221.
88. Burkert, Till, et al. "Giant magnetic anisotropy in tetragonal FeCo alloys." *Physical review letters* 93.2 (2004): 027203.
89. Gao, T. R., et al. "Combinatorial exploration of rare-earth-free permanent magnets: Magnetic and microstructural properties of Fe-Co-W thin films." *Applied Physics Letters* 102.2 (2013): 022419.

90. Néel, Louis, et al. "Magnetic properties of an iron—Nickel single crystal ordered by neutron bombardment." *Journal of Applied Physics* 35.3 (1964): 873-876.
91. Park, J. H., et al. "Saturation magnetization and crystalline anisotropy calculations for MnAl permanent magnet." *Journal of Applied Physics* 107.9 (2010): 09A731.
92. Zhou, Lin, et al. "Architecture and magnetism of alnico." *Acta Materialia* 74 (2014): 224-233.
93. Mukhamedov, B. O., A. V. Ponomareva, and I. A. Abrikosov. "Spinodal decomposition in ternary Fe-Cr-Co system." *Journal of Alloys and Compounds* 695 (2017): 250-256.
94. Gandha, Kinjal, Jeotikanta Mohapatra, and J. Ping Liu. "Coherent magnetization reversal and high magnetic coercivity in Co nanowire assemblies." *Journal of Magnetism and Magnetic Materials* 438 (2017): 41-45.
95. Poudyal N, Gandha K, Elkins K, Liu JP. Anisotropic SmCo5/FeCo core/shell nanocomposite chips prepared via electroless coating. AIMS Mater Sci. 2015;2(3):294
96. Gandha, Kinjal, et al. "Synthesis and characterization of FeCo nanowires with high coercivity." *Nanotechnology* 26.7 (2015): 075601.
97. Gandha, Kinjal, et al. "Effect of $RuCl_3$ on Morphology and Magnetic Properties of CoNi Nanowires." *IEEE transactions on magnetics* 49.7 (2013): 3273-3276.
98. Ohnuma, Ikuo, et al. "Phase equilibria in the Fe–Co binary system." *Acta Materialia* 50.2 (2002): 379-393.
99. Riani, Paola, Katarzyna Sufryd, and Gabriele Cacciamani. "Critical assessment and experimental investigation of Co–Ni–Ti phase equilibria." *Calphad* 44 (2014): 26-38.

100. Cormary, Benoit, et al. "Concerted growth and ordering of cobalt nanorod arrays as revealed by tandem in situ SAXS-XAS studies." *Journal of the American Chemical Society* 138.27 (2016): 8422-8431.

101. Ung, Diane, et al. "CoNi nanowires synthesized by heterogeneous nucleation in liquid polyol." *Advanced Materials* 17.3 (2005): 338-344.

102. Kneller, Eckart F., and Reinhard Hawig. "The exchange-spring magnet: a new material principle for permanent magnets." *IEEE Transactions on Magnetics* 27.4 (1991): 3588-3560.

103. Schrefl, Thomas, H. Kronmüller, and Josef Fidler. "Exchange hardening in nano-structured two-phase permanent magnets." *Journal of magnetism and magnetic materials* 127.3 (1993): L273-L277.

104. Carnevale, David J., Michael Shatruk, and Geoffrey F. Strouse. "Ligand Passivated Core–Shell FePt@ Co Nanomagnets Exhibiting Enhanced Energy Product." *Chemistry of Materials* 28.15 (2016): 5480-5487.

105. Zeng, Hao, et al. "Tailoring magnetic properties of core⁄ shell nanoparticles." *Applied Physics Letters* 85.5 (2004): 792-794.

106. Nandwana, Vikas, et al. "Bimagnetic nanoparticles with enhanced exchange coupling and energy products." *Journal of Applied Physics* 105.1 (2009): 014303.

107. Mrad, K., et al. "Control of the crystal habit and magnetic properties of Co nanoparticles through the stirring rate." *CrystEngComm* 19.25 (2017): 3476-3484.

108. Du Plessis, H. E., et al. "Stacking disorder in silicon carbide supported cobalt crystallites: an X-ray diffraction, electron diffraction and high resolution electron microscopy study." *Physical Chemistry Chemical Physics* 18.43 (2016): 30183-30188.

109. Coey, John MD. *Magnetism and magnetic materials*. Cambridge university press, 2010.